

Force sensing with nanowire cantilevers

F. R. Braakman^{1*} and M. Poggio¹

1: University of Basel, Klingelbergstrasse 82, 4056 Basel, Switzerland

(Dated: January 18, 2019)

Nanometer-scale structures with high aspect ratio such as nanowires and nanotubes combine low mechanical dissipation with high resonance frequencies, making them ideal force transducers and scanning probes in applications requiring the highest sensitivity. Such structures promise record force sensitivities combined with ease of use in scanning probe microscopes. A wide variety of possible material compositions and functionalizations is available, allowing for the sensing of various kinds of forces with optimized sensitivity. In addition, nanowires possess quasi-degenerate mechanical mode doublets, which has allowed the demonstration of sensitive vectorial force and mass detection. These developments have driven researchers to use nanowire cantilevers in various force sensing applications, which include imaging of sample surface topography, detection of optomechanical, electrical, and magnetic forces, and magnetic resonance force microscopy. In this review, we discuss the motivation behind using nanowires as force transducers, explain the methods of force sensing with nanowire cantilevers, and give an overview of the experimental progress and future prospects of the field.

Contents

I. Introduction	1
II. Mechanics of nanowire cantilevers	2
A. Linear motion of a single mode	2
B. Linear motion of two orthogonal modes	6
C. Coherent two-mode dynamics	7
D. Non-linear motion	7
III. Force sensing with nanowire cantilevers	8
A. Force sensitivity	8
B. Displacement detection	10
IV. Force microscopy with nanowire cantilevers	12
A. Optical force sensing	12
B. Electrical force sensing	13
C. Magnetic force microscopy	14
D. Magnetic resonance force microscopy	15
V. Outlook	17
References	18

I. INTRODUCTION

Recent years have seen a dramatic reduction in the size of mechanical elements that can be used as mass and force sensors. For the most sensitive applications, micro-processed Si cantilevers are starting to give way to bottom-up fabricated structures such as nanowires (NWs) and carbon nanotubes (CNTs). Bottom-up processes rely on self-assembly or driven self-assembly and allow for the production of nanometer-scale structures with atomic-scale precision. This trend towards miniaturization is not arbitrary: smaller mechanical transducers are inherently more sensitive. At the same time, atomic-scale control in the growth of such structures presents the opportunity to drastically reduce defects, improving mechanical quality and therefore also ultimate detection sensitivity.

Among the large variety of bottom-up nanostructures, NW cantilevers are particularly promising mechanical sensors due to their high aspect ratio. A long and thin NW that is clamped on one end forms an ideal scanning probe, making it amenable to a number of sensitive nanometer-scale imaging problems. At the same time, its symmetric cross-section results in orthogonal flexural mode doublets that are nearly degenerate. These modes allow a NW to be used as a kind of nanometer-scale force compass [1], such that both the magnitude and direction of a force can be measured. When the NW axis is oriented perpendicular to a sample surface, i.e. in the pendulum geometry, this enables the vectorial transduction of lateral forces. Moreover, the pendulum geometry allows a significant reduction of surface-induced dissipation compared to the more conventional parallel configuration. Furthermore, epitaxial growth allows the realization of NWs from a number of materials as well as heterostructures of such materials. In fact, due to their large surface-to-volume ratio, NWs are able to accommodate larger strain than conventional epitaxial films, allowing for the dislocation-free combination of materi-

*Author to whom correspondence should be addressed. Electronic mail: floris.braakman@unibas.ch.

als with large lattice mismatch [2].

The application of NWs to force sensing is proving particularly apt. As highly sensitive scanning probes, NW sensors have the ability to reveal subtle force fields with high spatial resolution. Unlike conventional atomic force microscopy (AFM), which reveals large, close-range forces – in some cases with atomic resolution – NWs are adept at discerning weak interactions. Ultra-low intrinsic mechanical losses make NWs excellent probes of tip-sample dissipation, a contrast which can be used to observe phase transitions as well as the local density of states [3–5]. The capability of nearly symmetric NWs to transduce lateral forces in two directions allows for imaging the full vectorial character of force fields. In particular, this enables the distinction of non-conservative forces, such as optical or frictional forces, from conservative ones, such as those arising from an electrical potential. Functionalized with a magnetic tip, a NW cantilever forms an excellent probe for the subtle magnetic field patterns produced by nanometer-scale magnetization textures such as domain walls, vortices, and skyrmions; superconducting vortices; mesoscopic transport in two-dimensional systems; and small ensembles of nuclear spins. Although NW force sensors are just starting to be used for many of these applications, they have already been applied as the active sensors in some of the most sensitive and highest resolution magnetic resonance imaging experiments realized to date [6–8].

This review is structured as follows: Section II gives an introduction to the mechanical dynamics of NW cantilevers. We first describe in Section II A flexural motion in a single oscillation direction and with displacement amplitudes small enough such that motion remains linear. Next, in Section II B we consider flexural motion in two different oscillation directions and the effects of vectorial forces and spatial force derivatives. This provides the conceptual background for the detection of 2D forces and force derivatives. We then see that shear force derivatives can lead to coupling between oscillations in two directions. As shown in Section II C, such coupling can be used to implement coherent two-mode dynamics, reminiscent of the dynamics of a quantum two-level system. Finally, we treat non-linear regimes of motion in Section II D. In Section III A we discuss the high force sensitivity of NW cantilevers. In particular, we cover how the geometry of a NW impacts its force sensitivity. In Section III B we discuss optical methods of detecting NW displacement in two directions. In Section IV we give an overview of experimental progress thus far and of the capabilities of NW transducers for specific forces. We conclude the review with an outlook for NW force transducers in Section V.

II. MECHANICS OF NANOWIRE CANTILEVERS

In this section, we give an overview of the mechanical behavior of NW cantilevers. Both the geometry and the material composition play an important role in determining the mechanical response of a NW cantilever to externally applied forces and force gradients, through its displacement profile, resonance frequency, and energy dissipation. NWs differ from conventional cantilevers in possessing a nearly symmetric cross-section. As we will see, this property implies that it is possible to use NW cantilevers as bidimensional force sensors. It is therefore of key importance to carefully choose the right type of NW for a specific force sensing application. Fortunately, a wide variety of NWs has become available in the last decades, produced either through bottom-up methods or by a top-down approach. This offers researchers a choice of many materials, heterostructures combining different materials, and various types of functionalization such as integrated quantum dots or magnetic tips. Furthermore, fine control over the shape of NWs has been demonstrated, yielding NWs with a tunable diameter, length, and with a variety of different cross-sections. In Table I we list experimentally determined mechanical properties of various NW cantilevers found in literature.

In the following, we model the NW cantilever as a singly-clamped beam of length L and with a uniform cross-section along its length. Fig. 1a schematically indicates the relevant parameters describing a singly-clamped beam undergoing flexural motion in a plane. For the purposes of force sensing, we are primarily interested in flexural modes and we do not consider longitudinal and torsional vibrations, since these modes are comparatively stiff and consequently have much higher oscillation frequencies.

A. Linear motion of a single mode

The flexural eigenfrequencies and eigenmodes of a singly-clamped beam can be derived analytically using Euler-Bernoulli theory, which gives a valid approximation when L is much larger than the cross-sectional dimension and when rotational bending and shear deformation can be neglected [32]. For a beam with completely symmetric cross-section, the bending moment of inertia is independent of the oscillation direction. As a consequence, flexural motion takes place in an arbitrary direction. For very asymmetric beams, such as conventional cantilever force transducers, which are flat, thin, and long, the predominant flexural motion occurs in one direction. In both cases, we can approximate the flexural motion by considering motion in one dimension. In Section II B, we consider NWs with slightly asymmetric cross-sections, in which case we will generalize the formalism to take into account a second dimension

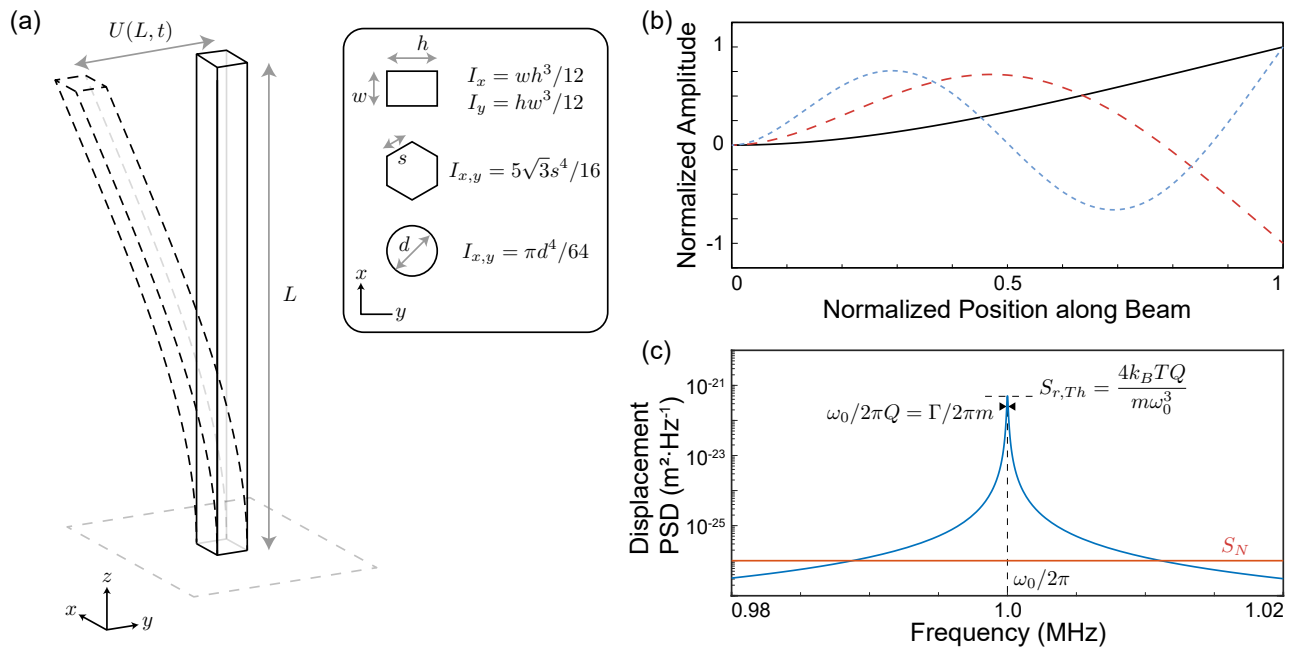


Figure 1: (a) Schematic overview of a singly clamped beam. Inset shows three cross-sectional beam shapes and corresponding moments of inertia. (b) Mode shapes of the first three flexural modes of a singly-clamped beam. (c) Plot of displacement power spectral density of a thermally driven resonator, for typical values of Q , ω_0 and $S_{F,Th}$. S_N is the power spectral density of measurement noise. Arrows indicate the half maximum.

of flexural motion.

As a starting point, we consider an idealized situation in which there is no dissipation and we do not take any driving forces into account. In this case, one can approximate the effect of a transverse force to be a torque perpendicular to both force and beam axis. An evaluation of the internal forces and torques along a flexing beam yields the following equation of motion:

$$E_Y I \frac{\partial^4 U(z,t)}{\partial z^4} + \rho A \frac{\partial^2 U(z,t)}{\partial t^2} = 0, \quad (1)$$

with z referring to the position along the beam, E_Y the Young's modulus of elasticity, I the second moment of area, which depends on the direction of flexural motion with respect to the cross-section, ρ the mass density, and A the cross-sectional area. This equation can be solved for the beam displacement $U(z,t)$, which can be separated into position- and time-dependent parts such that $U(z,t) = \sum_{n=1}^{\infty} r_n u_n(z) e^{i\omega_n t}$. Here we sum over the n particular solutions, or modes, with $u_n(z)$, r_n , and ω_n the one-dimensional shape, amplitude, and eigenfrequency associated with the n^{th} mode, respectively. In order for r_n to correspond to the amplitude of cantilever displacement, we use the normalization $|u_n(L)| = 1$. Note that this normalization entails that the n modes are orthogonal but not orthonormal.

Using the boundary conditions of a cantilever, i.e. that

one end of the beam is fixed ($u_n(0) = 0$) and not bending ($u'_n(0) = 0$) and that the other end is free to move (zero torque: $u''_n(L) = 0$ and zero transverse force: $u'''_n(L) = 0$), for small displacements Euler-Bernoulli theory yields the mode shapes:

$$u_n(z) = A \left[\left(\cos\left(\frac{\beta_n}{L}z\right) - \cosh\left(\frac{\beta_n}{L}z\right) \right) + \frac{\cos\beta_n + \cosh\beta_n}{\sin\beta_n + \sinh\beta_n} \left(\sinh\left(\frac{\beta_n}{L}z\right) - \sin\left(\frac{\beta_n}{L}z\right) \right) \right], \quad (2)$$

with A a normalization constant and β_n the dimensionless wavenumber of mode n . Fig. 1b shows the first three of these flexural mode shapes. The modes $u_n(z)$ can now be used in Eq. (1), resulting in the eigenfrequencies:

$$\omega_n = \frac{\beta_n^2}{L^2} \sqrt{\frac{E_Y I}{\rho A}} \quad (3)$$

Table II lists values of β_n and normalized values of the eigenfrequencies.

The eigenmodes and eigenfrequencies of Eq. (2) and Eq. (3) correspond to the ideal case of a cantilever without dissipation and without specifying any external transverse forces. To describe realistic time-dependent behavior of the beam, we must also include dissipation and external driving forces. Dissipation can be characterized by a quality factor, which is defined as

Material	Cross-section	d (nm)	L (μm)	$\omega/2\pi$ (kHz)	k (N/m)	Q	Ref.
GaAs/AlGaAs	Hexagonal	350	25	417	$1 \cdot 10^{-2}$	50,000 (4 K)	[9, 10]
GaAs	Hexagonal	234	16.8	598	$8.3 \cdot 10^{-3}$	46,553 (4 K)	[11]
GaAs	Hexagonal	100	<25	1,197	$8.3 \cdot 10^{-3}$	4,900 (RT)	[12]
GaAs/AlGaAs	Hexagonal	390	20	795	$9 \cdot 10^{-2}$	6,700 (4K)	[13]
GaAs	Hexagonal	130	14.5	465	-	2,000-3,000 (RT)	[14]
InAs	Hexagonal	60-80	4-5.5	2,023.9	$3.6 \cdot 10^{-3}$	1,752 (RT)	[15]
SiC	Circular	150	52	113	$4 \cdot 10^{-4}$	2,890 (RT)	[1]
SiC	Circular	200	50	78	$1.5 \cdot 10^{-4}$	1,000 (RT)	[16]
SiC	Circular	120	165	6.7	$3 \cdot 10^{-6}$	3,000 (RT)	[17]
SiC	Circular	284	128	33	-	36,000 (RT)	[18]
SiC	Circular	206	93	43	-	159,000 (RT)	[18]
SiC	Circular	50	7	1,519	-	2,500 (RT)	[19]
SiC	Circular	300	6	6,140	1.5	33 (RT, Air)	[20]
Si	Circular	44	14.4	210.5	$2.8 \cdot 10^{-5}$	9,250 (RT)	[21]
Si	Circular	46	12.9	273	$6.6 \cdot 10^{-5}$	7,250 (RT)	[21]
Si	-	35	15	1,060	$6.5 \cdot 10^{-4}$	25,000 (8 K)	[6]
Si	-	50	15	333	$1.5 \cdot 10^{-4}$	18,000 (6 K)	[7]
Si	Circular	50	15	197.5	$2.0 \cdot 10^{-5}$	3,000 - 3,500 (RT)	[22]
Si	Elongated circular	60, 80	20	342	$1 \cdot 10^{-4}$	8,150 (4K)	[8]
Si	Hexagonal	100-300	5-10	2,000-6,000	-	2,000 (RT)	[23]
Si	Hexagonal	165	12.7	1,772.4	-	3,000 (RT)	[24]
Si	Hexagonal	90	9.3	2,504.3	-	3,000 (RT)	[24]
Si	Hexagonal	100-200	6-8	3,500 - 4,000	$2.4 - 5 \cdot 10^{-2}$	3,000-3,500 (RT)	[25]
Si	Hexagonal	150 (clamp), 60 (tip)	11.3	2,480	-	-	[26]
Si	Hexagonal	39-400	2-20	1,000 - 12,000	-	3,000-25,000 (RT)	[27]
Si (metallized)	Hexagonal	142	2.25	200,000	110.3	2,000 (25 K)	[28]
Si (metallized)	Hexagonal	118	2.1	188,000	62.9	2,500 (25 K)	[28]
Si	Hexagonal	81	1.69	215,000	31.4	5,750 (25 K)	[28]
Si	Hexagonal	74	2.77	80,000	6.0	13,100 (25 K)	[28]
CNT	Circular	50	18	270	$\sim 10^{-4}$	250 (RT)	[29]
CNT	Circular	1 - 3	5	38,178.5	$4.5 \cdot 10^{-8}$	2,245 (RT)	[30]
CNT	Circular	4	1.2	5,955	$2.1 \cdot 10^{-5}$	-	[31]
CNT	Circular	-	-	363.5	$4.8 \cdot 10^{-6}$	571 (RT)	[31]

Table I: Experimentally determined parameters of singly-clamped NW cantilevers. Here the diameter d is the average cross-sectional width and $\omega/2\pi$ is the average frequency of the fundamental flexural mode doublet. The quality factor Q is the average value of the fundamental flexural mode doublet, taken for a freestanding NW, far from any sample surface and measured at low ambient pressures. RT stands for room temperature.

the ratio between the total stored energy of a resonator and the energy loss per cycle: $Q = 2\pi E/\Delta E$. In terms of the displacement, Q is a dimensionless constant describing exponential decay: $U(z, t) = \sum_{n=1}^{\infty} u_n(z) e^{i\omega_n t} e^{-\omega_n t/(2Q)} = \sum_{n=1}^{\infty} U_n(z) e^{i(1+i/(2Q))\omega_n t}$. Hence, we see that dissipation can be incorporated by

n	β_n	ω_n/ω_0
0	1.875	1.000
1	4.694	6.267
2	7.855	17.547
3	10.996	34.386
$n \geq 3$	$(n + 1/2)\pi$	$[(n + 1/2)\pi/\beta_0]^2$

Table II: Wave numbers β_n and normalized eigenfrequencies ω_n of a singly-clamped beam.

defining a new eigenfrequency $\omega'_{0n} = (1 + i/2Q)\omega_{0n}$.

Mechanical force sensors sensitively transduce forces and force gradients into a change of displacement or resonance frequency. To explain this in more detail, we now introduce transverse driving forces of the form $F_n(z, t) = F_{0n}(z) e^{i\omega_n t}$. For times long compared to transient time scales ($t \gg Q_n/\omega_n$), the displacement of the beam follows the driving force and has the form $U(z, t) = \sum_{n=1}^{\infty} U_n(z) e^{i\omega_n t}$. In the following, we only consider the motion of the free end ($z = L$) of the cantilever. By adding $F_n(L, t)$ to the right-hand-side of Eq. (1), we can evaluate the complex displacement response of the free end of the cantilever as a function of driving fre-

quency ω_n as:

$$r_n(\omega_n) = F_n(\omega_n)\chi_n(\omega_n) \equiv \frac{F_n(\omega_n)}{m_{n,eff}} \frac{1}{\omega_{0n}^2 - \omega_n^2 + i\omega_{0n}^2/Q_n} \quad (4)$$

Here $F_n(\omega_n)$ is the Fourier transform of $F_n(L, t)$ and $\chi_n(\omega_n)$ the mechanical susceptibility of the NW cantilever. Note that the displacement response given by the mode shapes requires the use of a mode-dependent effective mass $m_{n,eff}$ rather than the cantilever mass in describing the dynamical behavior of the cantilever. This can be understood by considering that elements of the beam located closer to its clamped end react to a transverse force as if the local mass were higher than for elements closer to the free end. In fact, the effective mass is proportional to the square of the mode volume $m_{n,eff} = \frac{1}{|u_n(z_0)|^2} \int \rho(z)|u_n(z)|^2 dV$ and hence depends on the chosen normalization of $u_n(z)$ [33]. Furthermore, $m_{n,eff}$ depends on the position along the beam z_0 for which motion is evaluated. For the fundamental flexural mode using our normalization condition $|u_n(L)| = 1$, it has a minimum of $m_{0,eff} = M/4$ for $z_0 = L$, with M the cantilever mass. From here on we will use the notation $m \equiv m_{0,eff}$. Interestingly, Eq. (4) differs only slightly from the response of a simple harmonic oscillator, for which $i\omega_{0n}^2/Q_n$ is replaced by $i\omega_n\omega_{0n}/Q_n$. The difference is negligible for large values of Q_n and disappears when driving on resonance.

In the following, we will therefore approximate the dynamics of a mode of a singly-clamped NW cantilever with that of a driven damped harmonic oscillator, considering only the displacement of the free end of the NW and assuming near-resonant driving. For simplicity, from now, we only consider the fundamental flexural mode (typically the only one used in force sensing) and consequently we drop the subscript n . For small NW oscillation amplitudes, we can approximate the force F acting on the NW around its equilibrium displacement $r = 0$ as $F \approx F(0) + rF_r$, with $F_r \equiv \partial F/\partial r|_0$. Writing the displacement $r(t)$ of the tip of the nanowire in an equation of motion of a damped driven harmonic oscillator, we obtain:

$$m\ddot{r} + \Gamma\dot{r} + (k - F_r)r = F(0) + F_{Th}, \quad (5)$$

where k is the mode spring constant and dots indicate differentiation with respect to time. We see that spatial derivatives F_r of forces acting on the NW modify the effective spring constant of the NW. Stationary forces acting on the NW provide a static offset of the cantilever displacement, whereas time-dependent forces can drive the motion of the NW and change its displacement amplitude, through the spectral transfer function of the resonance shown in Eq. (4). The aim of most force sensing experiments is the measurement of the forces $F(0)$ and force derivatives F_r .

The remaining terms in Eq. (5), $\Gamma\dot{r}$ and F_{Th} , correspond to dissipation and thermal force noise, respectively.

Forces acting on the resonator typically do not only arise from controlled interactions, but also include components originating from the cantilever being in contact with a thermal bath. The noise in the resonator motion that results from this interaction is observable in the most sensitive force sensing measurements, and is what typically sets the limit to their sensitivity. We include further terms in the equation of motion that account for energy dissipation and noise arising from the resonator being in contact with a largely uncontrolled and fluctuating environment of temperature T . This environment consists of a large number of degrees of freedom, such as those describing the motion of the molecules in the (typically highly diluted) fluid through which the nanowire moves and the phonon bath in the substrate to which the NW is attached through its clamping point. We use a statistical approach to include these effects in the equation of motion. The interactions with the environment can be decomposed into a rapidly fluctuating thermal force noise term F_{Th} and a slowly varying dissipation term proportional to the velocity of the resonator, $\Gamma\dot{r}$ (see Reif [34]), with $\Gamma = m\omega/Q$. While in thermal equilibrium, these two terms are related through the fluctuation-dissipation theorem [35], resulting in:

$$\Gamma = \frac{1}{2k_B T} \int_{-\infty}^{\infty} \langle F_{Th}(t)F_{Th}(t+s) \rangle ds, \quad (6)$$

where k_B is the Boltzmann constant and the brackets $\langle \dots \rangle$ indicate that an ensemble average is taken, here used in the correlation function $\langle F_{Th}(t)F_{Th}(t+s) \rangle$, with t and $t+s$ different points in time. To further describe the fluctuating force term $F_{Th}(t)$, we use the power spectral density (PSD). We define the force PSD $S_F(\omega)$ as the Fourier transform of the force correlation function:

$$S_F(\omega) = 2 \int_{-\infty}^{\infty} \langle F(t)F(t+\tau) \rangle e^{i\omega\tau} d\tau, \text{ for } 0 < \omega < \infty \quad (7)$$

Here we defined $S_F(\omega)$ to be single-sided: since $\langle F_{Th}(t)F_{Th}(t+s) \rangle$ is real, its Fourier transform is even. This allows us to only take into account positive values of ω in Eq. (7), provided we multiply the integral by 2. Furthermore, note that from the inverse Fourier transform of Eq. (7) we can find specifically that $\langle F(t)^2 \rangle = \frac{1}{2\pi} \int_0^{\infty} S_F(\omega) d\omega$. Correlations in a thermal bath (other than those taken into account for damping) usually exist only for extremely short times (typically $< 10^{-13}$ s). Therefore, for thermal noise we can assume $\langle F_{Th}(t)F_{Th}(t+s) \rangle = 2\Gamma k_B T \delta(s)$, resulting in the white single-sided force PSD $S_{F,Th} = 4k_B T \Gamma$.

The single-sided displacement PSD $S_r(\omega)$ can be similarly expressed by combining the amplitude response

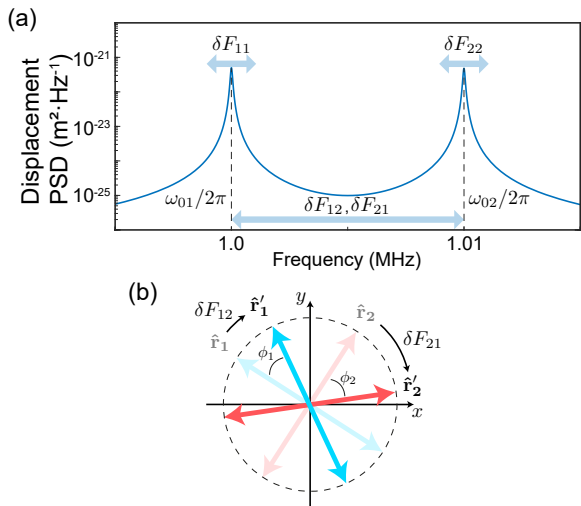


Figure 2: (a) Plot of thermal displacement PSD of a nearly-degenerate mode doublet. Arrows indicate the effect of the force derivatives F_{ij} on the resonant frequencies. (b) Schematic picture of rotation of mode directions under the influence of off-diagonal force derivatives F_{12} and F_{21} . Modes 1, 2 oscillate in the directions of the unit vectors $\hat{\mathbf{r}}_{1,2}$. The force derivatives δF_{12} and δF_{21} rotate the mode oscillation directions to point along the new unit vectors $\hat{\mathbf{r}}'_{1,2}$.

function of Eq. (4) with Eq. (7) as:

$$\begin{aligned}
 S_r(\omega) &= 2 \int_{-\infty}^{\infty} \langle r(t)r(t+\tau) \rangle e^{i\omega\tau} d\tau, \text{ for } 0 < \omega < \infty \\
 &= S_F(\omega) |\chi|^2(\omega) = \frac{S_F(\omega)}{m^2} \frac{1}{(\omega_0^2 - \omega^2)^2 + \omega_0^4/Q^2}
 \end{aligned} \quad (8)$$

We see that the mechanical resonator acts as a filter on the driving force, with $\chi(\omega)$ the filter transfer function. An important example of this filtering effect is that spectrally white force noise results in displacement noise with a nearly Lorentzian spectrum with a maximum of $S_{r,Th} = 4k_B T Q / m \omega_0^3$. As discussed in Section III A, this thermally induced displacement noise is what ultimately limits the sensitivity of force detection. Finally, we note that thermally induced phase noise (see Refs.[32, 36] for a thorough treatment) similarly limits the frequency stability of a mechanical resonator[37].

B. Linear motion of two orthogonal modes

For any cross-section that is symmetric around its center point, the moments of inertia I_x and I_y are equal, resulting in degenerate eigenmodes. The flexural oscillation direction in the plane is arbitrary in this case. Then the formalism of a single mode direction as discussed in the previous subsection suffices to describe the motion. However, small asymmetries in

the cross-section or in the clamping conditions [21] lift this degeneracy and split each mode into a doublet of modes oscillating along orthogonal directions $\hat{\mathbf{r}}_1$ and $\hat{\mathbf{r}}_2$ (see Fig. 2). For the fundamental flexural mode of NW cantilevers, this results in a doublet with resonance frequencies that are typically split by a small fraction of the resonance frequencies, but many times the resonance linewidths. Several groups working with NW force sensors have observed orthogonal modes with frequency splittings of the order of $10^3 - 10^4$ Hz. Moreover, similar orthogonal flexural modes can arise in doubly-clamped beams and have been observed, for example, in carbon nanotubes and SiN etched beams [38–40]. The use of such mode doublets as a way to realize bidimensional force sensing forms a major motivation for using NW cantilevers as force transducers and we will treat it in detail in this review. The mechanical dynamics of these mode doublets are very similar to that of two coupled modes and we can therefore apply the formalism of the previous subsection generalized to two modes.

Taking into account both orthogonal modes, the equation of motion can now be written in vectorial form as:

$$m\ddot{\mathbf{r}} + \mathbf{\Gamma} \cdot \dot{\mathbf{r}} + \mathbf{K} \cdot \mathbf{r} = \mathbf{F}(0) + \mathbf{F}_{Th} \quad (9)$$

Here the displacement and forces are vectors defined in the basis of the two mode directions $\hat{\mathbf{r}}_1$ and $\hat{\mathbf{r}}_2$, i.e. $\mathbf{r} \equiv \begin{pmatrix} r_1 \\ r_2 \end{pmatrix}$, $\mathbf{F}(0) \equiv \begin{pmatrix} F_1(0) \\ F_2(0) \end{pmatrix}$, and $\mathbf{F}_{Th} \equiv \begin{pmatrix} F_{Th,1} \\ F_{Th,2} \end{pmatrix}$. The effective mass m is taken to be equal for the two modes (see for experimental verification of this the Supplementary Information of Ref.[1]), and r_i are the mode displacements. $F_{Th,i}$ and F_i represent thermal force noise and other external forces acting on each of the two modes, respectively. We use the small-displacement approximation around $r_i = 0$, $F_i \approx F_i(0) + r_j \frac{\partial F_i}{\partial r_j} |0$. Furthermore, we define the dissipation and effective spring constant matrices $\mathbf{\Gamma} \equiv \begin{pmatrix} \Gamma_1 & 0 \\ 0 & \Gamma_2 \end{pmatrix}$ and $\mathbf{K} \equiv \begin{pmatrix} k_1 - F_{11} & -F_{21} \\ -F_{12} & k_2 - F_{22} \end{pmatrix}$. We write the four spatial force derivatives in shorthand notation as $F_{ij} \equiv \frac{\partial F_i}{\partial r_j} |0$, with $i, j \in \{1, 2\}$.

We see that the force derivatives F_{ij} cause a change in the spring constant of each mode, similar to the single-mode case. The off-diagonal elements of \mathbf{K} linearly couple the two modes, resulting in two new hybridized modes. The eigenvalues of the hybridized modes obtained by diagonalizing the \mathbf{K} matrix can be expressed as the modified spring constants (for $\Gamma_i/2m \ll \sqrt{k_i/m}$):

$$\begin{aligned}
 k'_{1,2} &= \frac{1}{2} \left[k_1 + k_2 - F_{11} - F_{22} \right. \\
 &\quad \left. \pm \sqrt{(k_1 - k_2 - F_{11} + F_{22})^2 + 4F_{12}F_{21}} \right]. \quad (10)
 \end{aligned}$$

The modified eigenfrequencies then follow as $\omega'_{0,i} = \sqrt{k'_i/m}$. The directions of the corresponding new eigen-

modes can be written as:

$$\begin{aligned}\hat{\mathbf{r}}'_1 &= \frac{1}{\sqrt{(k_2 - F_{22} - k'_1)^2 + F_{12}^2}} \begin{pmatrix} k_2 - F_{22} - k'_1 \\ F_{12} \end{pmatrix}, \\ \hat{\mathbf{r}}'_2 &= \frac{1}{\sqrt{(k_1 - F_{11} - k'_2)^2 + F_{21}^2}} \begin{pmatrix} F_{21} \\ k_1 - F_{11} - k'_2 \end{pmatrix}\end{aligned}\quad (11)$$

We can further simplify Eq. (10) by making the assumption that the force derivatives are much smaller than the bare NW spring constants k_i , which is usually satisfied. This yields $k'_i \approx k_i - F_{ii}$ and the following expression for the diagonal elements of the force derivative matrix:

$$F_{ii}|_{r_i=0} \approx -2k_i \Delta\omega_{0,i}/\omega_{0,i}. \quad (12)$$

Here $\Delta\omega_{0,i}$ is the frequency shift of mode i induced by the force derivatives. Using the same approximation, the off-diagonal elements of the force derivative matrix (shear force derivatives) can be deduced from the angle ϕ_i (see Fig. 2b) between the mode direction $\hat{\mathbf{r}}'_i$ in the presence of the force derivatives and the bare mode direction $\hat{\mathbf{r}}_i$ to be:

$$F_{ij}|_{r_i=0} \approx |k_i - k_j| \tan(\phi_i) \text{ for } i \neq j. \quad (13)$$

Note that in the situation where the NW cantilever is very soft and strong force derivatives are probed, these approximations are not valid and expressions for F_{ii} and F_{ij} remain slightly more complicated. In this case, the effects of the external force field dominate over the intrinsic NW mechanical properties, and the new eigenmodes tend to align with the eigenvectors of the force derivative matrix[16].

Eq. (12) and Eq. (13) show that all in-plane force derivatives can be determined from measurements of the frequencies and oscillation angle of the two modes. The effect of F_{ij} on the two resonance frequencies is illustrated in Fig. 2a. Finally, we note that the hybridized modes remain orthogonal as long as only conservative forces are included, in which case $F_{12} = F_{21}$. For forces with a finite curl, such as those arising from optical or frictional forces, $F_{12} \neq F_{21}$ and orthogonality is not maintained. In this situation, the standard fluctuation-dissipation theorem is no longer a valid method of describing the interactions of the bimodal NW with a thermal environment and needs to be modified to include excess noise arising from the non-zero curl of \mathbf{F} [17]. An important further consequence of non-orthogonality is that it becomes impossible to distinguish a rotation of a mode from a change in mode temperature without a full vectorial read-out as described in Section III B.

The forces \mathbf{F} and \mathbf{F}_{Th} are two-dimensional generalizations of the forces acting on a single mode. As for a single mode, stationary forces \mathbf{F}_1 and \mathbf{F}_2 yield a static offset in the NW displacement, now for each mode direction. Time-dependent forces drive the modes, leading to mode displacements given by a generalization of Eq. (4):

$$r'_i(\omega) = \mathbf{F}(\omega) \cdot \hat{\mathbf{r}}'_i \chi'_i(\omega) \text{ with } i, j \in \{1, 2\}, \quad (14)$$

with $\hat{\mathbf{r}}'_i$ the unit vector along the oscillation direction and $\chi'_i(\omega)$ the susceptibility of mode i , respectively. As described before, the force derivatives acting on the NW lead to the modified spring constants k'_i and mode directions $\hat{\mathbf{r}}'_i$, resulting in the new susceptibilities $\chi'_i(\omega)$. Fig. 3b and c show how measurements of the displacement amplitudes and phases of both modes as a function of driving frequency can be used to reconstruct the full vectorial driving force.

C. Coherent two-mode dynamics

As mentioned in the above, the shear force derivatives F_{ij} , with $i \neq j$, couple the motion in the two modes. Interestingly, the resulting hybridized eigenmodes display coherent dynamics similar to that of quantum two-level systems. Coherent two-mode phenomena such as avoided mode crossings and Rabi oscillations have been observed in classical systems including modes of optical ring resonators[41] and recently also in nanomechanical resonators [39, 40, 42]. Furthermore, coupling of the orthogonal fundamental flexural modes of a NW cantilever was demonstrated through the measurement of avoided crossings of the mode frequencies [10], see Fig. 4a. In the same experiment, Rabi oscillations were demonstrated through the use of time-dependent electric field derivatives, see Fig. 4b. The NW was embedded in a scanning probe setup, which made it possible to tune both the coupling strength and the Rabi frequency by positioning the NW inside the electric field provided by the sample. Such coherent two-mode dynamics does not only illustrate the similarities of quantum and classical wave mechanics, but can also be used to enhance force sensing. In particular, coherent pulse sequences reminiscent from quantum control techniques[43], such as Hahn echoes and dynamical decoupling, give the potential to increase the frequency stability of mechanical sensors, ultimately leading to higher sensitivities. Furthermore, such pulsing techniques make it possible to implement a range of noise spectroscopy methods in classical force and mass sensing[43].

D. Non-linear motion

In force sensing, non-linear regimes of motion are typically avoided. However, in nanomechanical resonators such as NWs, non-linear motion typically arises already for modest driving amplitudes and therefore needs to be considered. Moreover, non-linearities can be put to good use, since they allow to implement amplification of forces through parametric driving[32] or through mechanical mixing[44]. Furthermore, parametric driving allows to increase the ratio of transduced force signal to read-out noise[45]. In the last part of this section, we treat the situation in which the displacement of the NW cannot be considered to be small anymore and non-linear terms

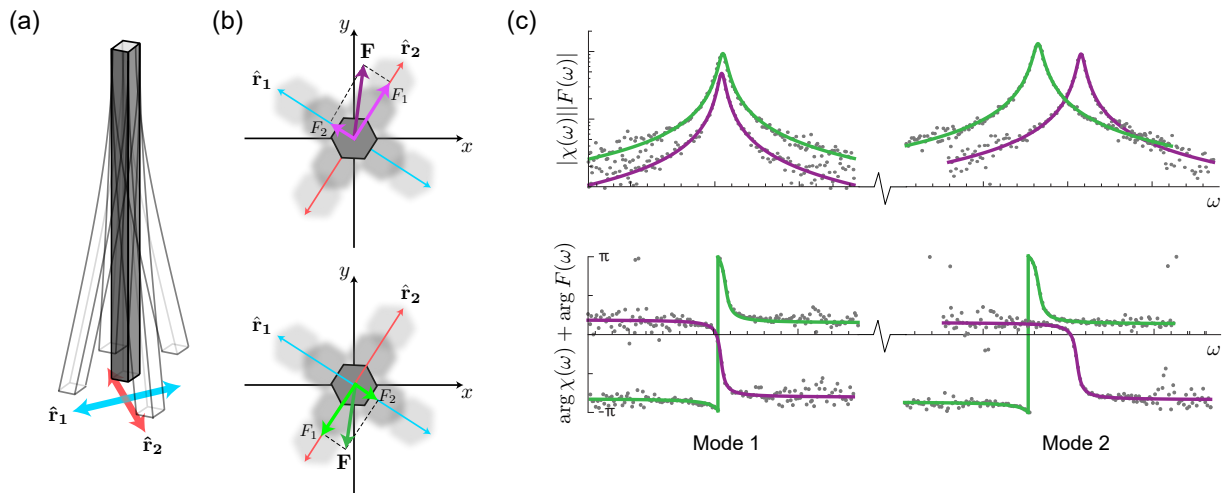


Figure 3: (a) Illustration of two orthogonal flexural modes in a NW cantilever. (b) Illustration of projection of vectorial forces onto mode directions, in the absence of spatial force derivatives. (c) Displacement amplitude and phase response of two modes as a function of driving frequency. The green and purple curves correspond to the response to the two forces indicated in (b) with the same colors. The displacement of each mode allows to extract the magnitude of the force component along that mode direction. The phase response of this mode with respect to the driving then allows to determine the sign of the force component along each mode direction. Adapted from Ref.[9]

need to be added to the equation of motion that depend on the oscillation amplitude.

It can be shown that for the fundamental flexural mode of a cantilever, the geometric non-linearity, associated with the lengthening of the beam as it flexes, dominates over other types of non-linearity, such as inertial non-linearity[46–48]. The first relevant higher-order terms are a damping term, as well as an effective spring constant term, that both have a quadratic dependence on the oscillation amplitude. For a single mode, this results in the following equation of motion [49]:

$$m\ddot{r} + \Gamma\dot{r} + \eta r^2\dot{r} + kr + \alpha r^3 = F(0) + F_{Th}(0) + F_r r \quad (15)$$

The coefficient α parametrizes the strength of the cubic (Duffing) non-linearity, whereas η is the coefficient of non-linear damping (note that here we contracted m into α and η). For weak damping and weak anharmonicity, other second- and third-order terms can be absorbed into the coefficients α and η [50, 51]. The equation of motion Eq. (15) leads to an amplitude response as a function of driving frequency with a characteristic shark-fin shape, as shown in Figure 5. This lineshape is a consequence of Eq. (15) having two stable solutions within a certain frequency range. This bistability leads to the switching phenomena seen for high driving amplitudes at the right flank of the response peak (Fig. 5 (a)). Which of the two solutions is realized, is determined by the initial conditions, and mechanical hysteresis can be observed when adiabatically sweeping the driving frequency or driving amplitude up and down (Fig. 5 (b) and (c)). When α is positive (negative), the Duffing non-linearity increases

(decreases) the effective spring constant with increasing driving amplitude, thus stiffening (softening) the motion. The value and sign of α has been demonstrated to be tunable both through the shape of the NW [14], as well as through feedback using a nearby gate electrode [22]. The non-linear damping term has the effect of decreasing the shift of the frequency of maximum response amplitude due to the Duffing non-linearity, as well as decreasing the size of the hysteresis loop. Non-linear damping has so far not been demonstrated for NW cantilevers. Finally, note that the dependence of mode frequencies on the displacement can lead to coupling between the two orthogonal modes. Considering only the Duffing non-linearity, the non-linear term for two modes becomes $\alpha|\mathbf{r}|^2\mathbf{r}$; this term induces a coupling between two modes. The coupling can be observed as a quadratic shift of a mode frequency as a function of the oscillation amplitude of the other mode (see Fig. 5 (d)).

Notwithstanding its potential for force amplification, non-linear motion has so far not been used in experiments on force sensing with NW cantilevers. In the following sections, we therefore only consider the operation of NW force transducers in a linear regime of motion.

III. FORCE SENSING WITH NANOWIRE CANTILEVERS

A. Force sensitivity

The key component in any force microscope is the force sensor. This device consists of a mechanical transducer,

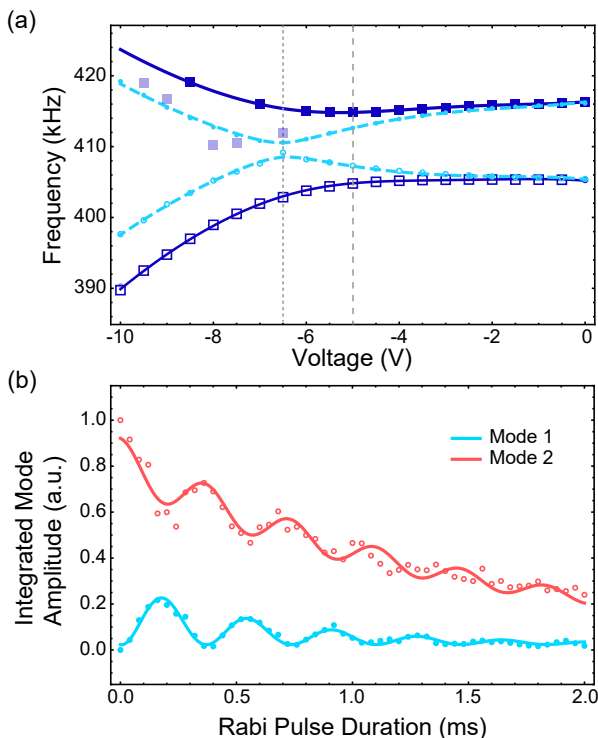


Figure 4: (a) Mode frequencies as a function of voltage applied over two nearby surface gates, for two different positions of the NW tip inside the electric field. (b) Integrated displacement amplitudes of both modes as a function of Rabi pulse duration. Points indicate measured data, solid lines are fits to the data. Note that the offset in the measured Rabi oscillations is due to thermal excitation of the mode. Different offsets result from the difference in angle of the two mode directions with the read-out vector. Adapted from Ref.[10].

used to convert force into displacement, and an optical or electrical displacement detector. Although early AFM transducers were simply pieces of gold or aluminum foil [52], specially designed and mass-produced Si cantilevers soon became the industry standard and led to improved resolution and force sensitivity [53]. These micro-processed devices are now cheap, readily available, and designed – depending on the target application – to have a variety of features including coatings, electrical contacts, or magnetic tips.

Conventional top-down cantilevers are well-suited for the measurement of the large forces and force gradients present on the atomic-scale. Nevertheless, for some applications sensitivity to small forces is crucial. These range from mass detection, to cantilever magnetometry, to scanning measurements of friction forces, Kelvin probe microscopy, electric force microscopy, magnetic force microscopy (MFM), and force-detected magnetic resonance. This push towards higher sensitivity has generated an interest in using ever smaller mechanical force transducers, especially those made by bottom-up techniques.

The trend towards decreasing the size of mechanical

transducers is based on fundamental principles. Once the detection of a transducer’s displacement is optimized, the minimum detectable force F_{\min} is ultimately limited by the thermal force fluctuations acting on the transducer, whose PSD, as discussed in Section II A, is given by $S_{F,th}$. As a result,

$$F_{\min} = \sqrt{S_{F,th}} = \sqrt{4k_B T \Gamma}, \quad (16)$$

Optimizing sensitivity therefore involves reducing the operating temperature and the dissipation. Note that efforts aimed purely at increasing mechanical quality factor may not necessarily minimize F_{\min} . Work on so-called ‘damping dilution’, uses tension applied to strings or membranes to increase resonant frequency ω while holding Γ constant, thereby increasing Q [48, 54–57]. Although these methods do not improve F_{\min} , they do reduce the thermal decoherence time, which is important for experiments seeking to probe macroscopic quantum superposition states [58].

The sensitivity to a number of measurements is closely related to F_{\min} [59]. For example, the minimum detectable force gradient is given by $(\partial F/\partial x)_{\min} = F_{\min}/x_{\text{osc}}$, where x_{osc} is the root-mean-square oscillation amplitude of the transducer. Cantilever beams are also excellent torque transducers and, for some applications, torque is the measurement quantity of interest, e.g. in torque magnetometry. A cantilever’s thermally limited torque sensitivity is given by $\tau_{\min} = l_e F_{\min}$, where l_e is the effective length of the cantilever, which takes

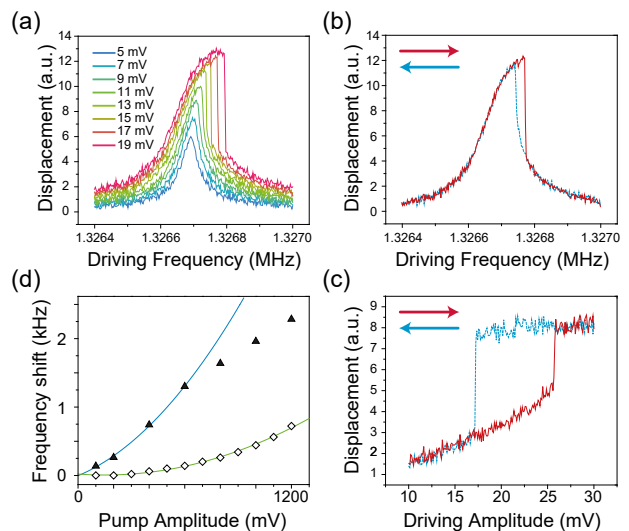


Figure 5: (a) Displacement as a function of driving frequency, for various amplitudes of piezoelectric driving. (b) Displacement as a function of driving frequency (at a driving amplitude of 17 mV), for two sweep directions (as indicated by arrows). (c) Displacement as a function of driving amplitude (at a driving frequency of 1.326 77 MHz), for two sweep directions. (d) Frequency shift of one mode as a function of amplitude of piezoelectric driving of orthogonal mode. Adapted from Ref.[44].

into account the shape of the flexural mode [60]. Finally, for experiments that measure energy dissipation, $\Gamma_{\min} = F_{\min}/(\omega_0 x_{\text{osc}})$.

In practice, this means that at a given temperature, a well-designed cantilever transducer must simultaneously have low $m\omega_0$ and large Q . In the limit of long and thin cantilever beam, the Euler-Bernoulli equations imply that $m\omega_0 \propto d^3/l$, where d is its diameter and l its length. For sensitive transducers, experiments show that Q is limited by surface-related losses, which lead to a linear decrease of Q with increasing surface-to-volume ratio, i.e. $Q \propto d$ [61]. As a result, we see that $\Gamma \propto d^2/l$, implying that long and thin cantilevers should be the most sensitive. In fact, a review of real transducers confirms this trend.

High mechanical resonance frequencies are also attractive for sensitive force transducers, since they allow for the measurement of fast dynamics and they decouple the sensor from common sources of noise. A prominent example is the additional noise experienced by a cantilever as its tip approaches a surface [62, 63]. This so-called non-contact friction is largely due to electronic fluctuations on the surface and typically has a $1/f$ -like frequency dependence. As a cantilever approaches a surface, Γ usually increases and its force resolution suffers. Such processes can be mitigated through the use of high-frequency cantilevers. When the resonant frequency of the mechanical oscillator is much higher than the characteristic frequency of the external noise, the resonator can be effectively decoupled from that noise.

A cantilever's angular resonance frequency is given by $\omega_0 \propto d/l^2$. Therefore, if we scale each of its dimensions uniformly by a factor β , we find that $\omega_0 \propto 1/\beta$, while $\Gamma \propto \beta$. Therefore, in order to simultaneously maximize ω_0 and minimize Γ , the entire structure should be scaled down. $F_{\min} \propto \beta^{1/2}$, while because of the additional contribution of the cantilever's effective length $l_e \propto \beta$, $\tau_{\min} \propto \beta^{3/2}$. Reducing all dimensions while preserving the aspect ratio of a long and thin cantilever beam should thus optimize its ultimate force and torque sensitivity. This necessity for further miniturization has positioned bottom-up techniques as the fabrication methods of the future.

In recent years, remarkable progress has been made in this direction with force sensors made from doubly clamped CNTs [64], suspended graphene sheets [65], and NW cantilevers [1, 9, 16]. In two separate papers, Moser et al. demonstrated the use of a CNT as a sensitive force sensor with a thermally limited force sensitivity of 12 zN/ $\sqrt{\text{Hz}}$ at 1.2 K in 2013 [38] and then of 1 zN/ $\sqrt{\text{Hz}}$ at 44 mK in 2014 [66]. Given their geometry, graphene resonators are extremely difficult to apply in scanning probe applications. Singly clamped NWs and CNTs on the other hand, when arranged in the pendulum geometry – that is, with their long axes perpendicular to the sample surface – are well-suited as scanning probes. Their orientation prevents the tip from snapping into contact [67]. When brought close to a surface, NWs experience ex-

tremely low non-contact friction [6], making near-surface (< 100 nm) force sensitivities around 1 aN/ $\sqrt{\text{Hz}}$. As a result, NWs have already been used as scanning probes in a variety of proof-of-principle experiments discussed in Section IV.

B. Displacement detection

As discussed above, the force transducer sets the fundamental sensitivity limits of any force sensor. However, for a force to be measured, the transducer's displacement must be detected. Therefore, in order to achieve the sensor's ultimate sensitivity, a displacement detection scheme sensitive enough to detect the transducers thermal motion is required. The displacement of conventional AFM cantilevers is measured through the deflection of a laser beam reflected off of the cantilever and onto a split photodetector. Although this scheme works well for cantilevers with flat surfaces large enough to specularly reflect a laser beam, it is not well-suited for NWs. Given their shape and sub-wavelength diameter, diffraction effects emerge and an alternative means of displacement detection must be employed.

To circumvent this challenge, researchers have developed a number of optical [25, 27, 68–71] and non-optical techniques, including electron beam [72], piezoresistive [73], magnetomotive [28], and capacitive [64, 74] displacement detection. None of these, however, are compatible with sensitive scanning probe microscopy (SPM) applications, in which the NW cantilevers thermal motion must be non-invasively detected while its tip is positioned close to the surface of a sample. Most recently, a pair of optical techniques based on optical interferometry or scattering have been shown to be compatible with SPM applications, while at the same time providing access to both the amplitude and direction of the NW displacement [1, 9, 11, 16, 21]. A technique in which the electron beam in a scanning electron microscope (SEM) is focused on a cantilever and the inelastically scattered electrons are detected also resolved thermal displacement fluctuations of a singly clamped CNT [31]. This scheme was subsequently integrated into a SPM with the CNT as the force transducer [29]. Due to its flexibility and relatively simple hardware required for its implementation, we will focus here on the optical techniques.

Using Mie scattering analysis, it can be shown that a NW positioned near the focus of an incident laser beam scatters sufficient light such that a measurement of optical transmission is sufficient to sensitively detect its displacement [75]. The technique uses the strong scattering intensity gradient as a function of the NW position in the plane perpendicular to its axis (xy -plane), to convert NW displacement into a change in optical transmission intensity I_T . The gradient of this intensity as a function of the NW position yields both the detection efficiency $\epsilon = |\nabla I_T(x, y)|$ in W/m and the direction along which displacement is detected $\hat{\mathbf{m}} = \nabla I_T(x, y)/|\nabla I_T(x, y)|$

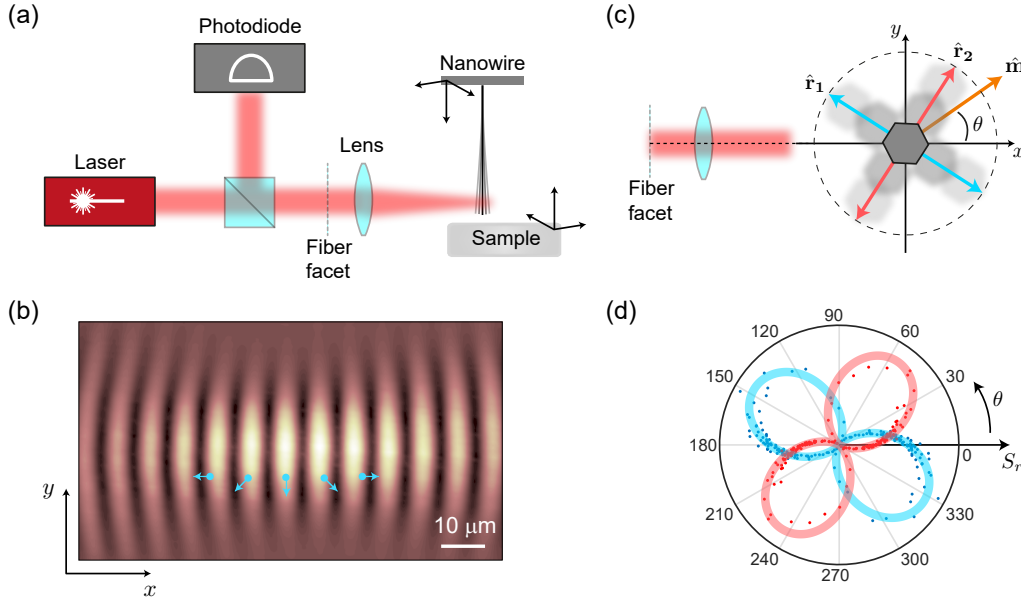


Figure 6: (a) Diagram of NW displacement detection setup. (b) Reflected intensity measured as a function of xy position of NW tip showing the interference fringes resulting from the low-finesse interferometer in the detection path. Arrows indicate the direction of the gradient of the intensity for different positions, determining the direction of the measurement vector. (c) Diagram illustrating mode directions and measurement vector. (d) NW displacement PSD as a function of measurement angle.

[1]. The measured displacement is therefore a projection of the displacement of the two flexural modes $m(t) = \hat{\mathbf{m}} \cdot (\mathbf{r}_1(t) + \mathbf{r}_2(t))$ along a direction that depends on the position of the NW in the beam waist. Using a split-photodiode detector, different response profiles can be obtained from the sum and difference of the two sensors. As a result, displacement signals along two perpendicular directions can be measured at the same time [16]. In this way, even with modest optical powers, the thermal displacement of the NW modes can be measured in two-dimensions. The detection can be used to fully characterize the response of each set of doublet flexural modes to external forces and force gradients. Ultimately, this vectorial information allows for the reconstruction of the full two-dimensional force field acting on the NW. In addition, the relative orientation of the doublet, i.e. whether these modes oscillate orthogonal to each other or not, carries information about whether the force field in which the NW is immersed is conservative or not [17].

Another version of this detection scheme uses the interference between light scattered back from the NW and light reflected from the cleaved end of an optical fiber to measure NW displacement [11, 76]. In this case, a fiber-based confocal reflection microscope is used to collect the light scattered from the NW, as shown in Fig. 6 (a). The fiber's end and the NW form a low-finesse Fabry-Perot cavity interferometer [9, 21], whose interferometric response depends on the position of the NW in the beam waist, as seen in Fig. 6 (b). A fast photo-receiver monitors variations in the reflected intensity I_R , allowing for the sensitive detection of NW motion. As before, the ef-

iciency $\epsilon = |\nabla I_R(x, y)|$ and the direction of the detected displacement $\hat{\mathbf{m}} = \nabla I_R(x, y) / |\nabla I_R(x, y)|$ depend on the variations of I_R as a function of the NW position in the optical waist [11]. In this case, along the cavity's axis, ∇I_R depends on an interference effect and therefore can have a very high ϵ , which can be improved by increasing the cavity finesse. Detection efficiency perpendicular to the cavity axis, on the other hand, depends on the narrowness of the optical waist. Using this method, the axis along which displacement is measured can be changed either by moving the NW within the optical waist or by tuning the laser excitation wavelength, which alters the interference pattern shown in Fig. 6 (b). As with the scattering based technique, this two-dimensional displacement detection technique allows for both angular and spectral tomography of a NW's flexural modes. As an example, the displacement power spectral density of a NW's thermally-excited fundamental mode doublet and its displacement power density as a function of the angle in the xy -plane are shown in Fig. 6 (d).

Both the optical transmission and the interferometric techniques have been successfully integrated into a SPM using a single NW as the force transducer. Although technical restrictions exist, such that there is sufficient optical access to the NW (e.g. on the length of NW and the distance of the scanning region from the sample edge), setups can be designed to work with most samples of interest.

IV. FORCE MICROSCOPY WITH NANOWIRE CANTILEVERS

Recently, several proof-of-concept experiments have been performed that demonstrate the potential of force microscopy with NW cantilevers. First experiments focused on developing the optical detection of NW displacement[21, 25, 26] with high enough precision to observe the NW's thermomechanical noise, as well as on characterizing the mechanical properties of NW cantilevers[12, 22, 44]. The promise of ultralow dissipation motivated researchers to implement NW cantilevers into scanning probe setups, for the sensitive detection of various types of forces. In a series of experiments[6, 7, 22], Nichol et al. first used Si NWs as transducers in magnetic resonance force microscopy, exploiting their high mechanical frequencies and low dissipation to improve the sensitivity and resolution in measurements of small numbers of nuclear spins.

As mentioned before, when used in the pendulum geometry, NW cantilevers enable scanning probe microscopy of lateral forces. Such a mode of operation is of great interest for the detection of for instance frictional forces[4] and for the detection of short-range non-central forces[77]. Although one-dimensional dynamic lateral force microscopy can be realized using the torsional mode of conventional AFM cantilevers [78–82], the ability to simultaneously image all vectorial components of nanoscale force fields is of great interest. Not only does it provide more information on tip-sample interactions, but it also enables the investigation of inherently 2D effects, such as the anisotropy or non-conservative character of specific interaction forces. This vectorial force sensing has now been demonstrated for a variety of types of interaction.

The first implementation of a vectorial NW force sensor was realized by Gloppe et al.[1] in an experiment where the optical force field of a laser beam focused onto a NW was mapped out. Optomechanical interactions lie at the basis of a very fruitful line of research in which quantum states of motion are studied using optical fields, for instance in optical resonators. To fully describe such optomechanical interactions, one needs to take into account their non-conservative nature, and their spatial mapping necessitates the use of a fully vectorial force sensor as described by Gloppe et al. Interestingly, this non-conservative character of the optomechanical interaction can induce strong coupling between orthogonal mechanical modes. Interestingly, the vectorial nature of the optomechanical interaction can induce strong coupling between orthogonal mechanical modes, which can lead to non-trivial forms of back-action on the NW motion.

In a next step, vectorial NW force sensors were implemented in scanning probe setups, in which the NW cantilever could be scanned over a sample surface[9, 16]. These setups allowed for the measurement of two-dimensional maps of the sample surface, in which forces

arising from Coulombic interactions, chemical bonding, and van der Waals interactions provide a topographic contrast. The NW cantilevers complement conventional AFM in providing a full determination of the four lateral force derivatives. Together, these experiments show the potential of NW cantilevers as ultrasensitive bidimensional force transducers and provide experimental quantification of sensitivities and resolution. Force sensitivities were measured to be in the $\text{aN Hz}^{-1/2}$ range. This is on par with or slightly better than sensitivities reached with conventional AFM. However, there is great potential for improvement of the force sensitivity, through optimization of NW geometry and surface properties. Spatial resolution was limited, as expected, by the NW tip diameter, which for these first experiments ranged between 100 and 350 nm. Also here, there is a clear route for improvement, since several types of NWs and nanotubes with tip diameters that are 10-100 times smaller have been grown.

A further exciting new development is the use of NW cantilevers with magnetic tips for sensitive and vectorial detection of magnetic forces. In recent years, there has been a flurry of activity in developing nanometer-scale magnetic imaging technology. These efforts are driven by a number of outstanding questions in spintronics – such as how to control magnetic skyrmions – and in mesoscopic transport – such as how current flows in topological insulators and two-dimensional materials. Scanning probe microscopy, in particular, has made remarkable improvements in both the sensitivity and resolution of magnetic imaging. Some of the most successful tools are magnetic force microscopy (MFM), spin-polarized scanning tunneling microscopy, as well as scanning magnetometers based on nitrogen-vacancy centers in diamond, Hallbars, and superconducting quantum interference devices (SQUIDs). Despite this progress, it is now becoming clear that nanomechanical sensors, in general, and NWs in particular, provide a huge untapped opportunity in magnetic sensing. First results of NW MFM were obtained using a NW with a magnetic segment grown at its tip[11].

A. Optical force sensing

Optical setups used to detect the displacement of a cantilever, be it based on interferometry or scattering of light, can also be applied to study optomechanical interactions. The NW cantilever with its two orthogonal flexural modes gives the opportunity to investigate the vectorial nature of optomechanical coupling. Gloppe et al. have performed such a study, by placing a NW cantilever inside the optical field of a laser beam tightly focused by a microscope objective with a high numerical aperture[1]. In this experiment, the optical intensity of the field was modulated with a frequency that was swept through both orthogonal mode resonant frequencies, providing driving forces through the optomechanical inter-

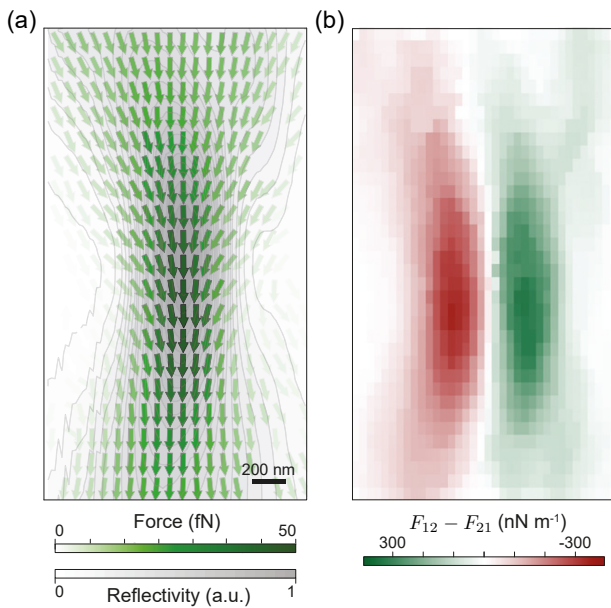


Figure 7: (a) Measured spatial map of optomechanical force field on NW tip placed inside focused laser beam. (b) Spatial map of the local curl derived from measurement displayed in (a). Adapted from Ref.[1].

action. A second, much weaker laser beam was used to probe the thermal force noise of the NW, allowing the determination of the direction of the NW modes following the method outlined in Section II B. The method of Fig. 3 was then used to acquire a map of the magnitude and direction of the in-plane optomechanical force. The force field of Fig. 7a shows a converging and diverging vector flow corresponding to the waist area of the focused laser beam. The optomechanical interaction is in general non-conservative and therefore the force field acting on the NW can possess a non-zero curl. The curl can be found by differentiating the vector force field and was determined to be maximum at the waist, on each side of the optical axis (see Fig. 7b). Furthermore, by measuring the delay between the laser intensity modulation and the NW response it was shown that the optomechanical force was in phase with the intensity modulation, as expected for a dissipative optomechanical coupling. The authors report a force sensitivity in the $\text{aN Hz}^{-1/2}$ range at room temperature.

B. Electrical force sensing

In scanning probe measurements of a sample surface, such as those made in conventional atomic force microscopy, the underlying sample-cantilever forces are typically of electrical origin. These forces include contributions from van der Waals forces and various other interactions of electrostatic origin. The measured forces closely follow the geometrical pattern of the

sample surface, enabling the reconstruction of sample topography. In contrast to conventional AFM, NW cantilevers arranged in the pendulum geometry allow for the measurement of vectorial topographical maps of sample surfaces through the measurement of in-plane forces and force derivatives. In two experiments[9, 16], researchers recently demonstrated the use of NW cantilevers to measure such topographical maps.

Fig. 8 shows various measurements involving a specific sample featuring 200 nm thick Au gate electrodes lithographically defined on a planar Si substrate. By scanning a NW cantilever over the sample surface, vectorial maps of the tip-sample forces and forces derivatives, as well as of the dissipation of both NW modes, were measured[9]. Fig. 8a-c show maps of in-plane spatial force derivatives F_{11} , F_{22} , and F_{12} (since electrical potentials are conservative, here $F_{21} = F_{12}$), through measurements of the frequency shift and oscillation direction of the two orthogonal flexural modes of the NW. The measured in-plane force derivatives can be integrated to produce a map of in-plane tip-sample forces, up to an integration constant corresponding to a constant force in the plane. Fig. 8d shows a map of the force field F_{int} extracted from such an integration and confirms that the measured forces are roughly perpendicular to the edges defined by the sample topography. Furthermore, Fig. 8e, f show maps of measured dissipations Γ_i , extracted from the mode linewidths. Dissipation was measured to be nearly isotropic in the plane and was affected mostly by the different materials and tip-sample spacing over electrodes and substrate. In principle however, the demonstrated ability to produce vectorial maps of dissipation moreover that NW cantilevers could find application in the study of anisotropic non-contact friction, which is important for instance for the study of superlubricity[83].

In a next step, the authors generated an alternating electric field $\mathbf{E}(\mathbf{r}, t)$ using the patterned electrodes to drive the motion of both NW modes. In this way, vectorial in-plane maps of the driving forces were obtained (see Fig. 8g, h), with a thermally limited sensitivity of $5 \text{ aN Hz}^{-1/2}$ at a temperature of 4 K. Two types of driving forces resulted from $\mathbf{E}(\mathbf{r}, t)$: $\mathbf{F}_q = q\mathbf{E}$ and $\mathbf{F}_p = -\nabla(\alpha|\mathbf{E}|^2)$. Here q is the net charge on the NW tip and α the polarizability of the NW. Since \mathbf{F}_q shows a linear dependence on the magnitude of the electric field, while that of \mathbf{F}_p is quadratic, these two forces are spectrally separated and could therefore be distinguished in measurement. Interestingly, such force measurements also allow the characterization of the NW itself. By comparing the magnitude of the measured forces with that of the applied electric field, the average values of the constants q and α could in this case be determined.

In a similar setting, Mercier de Lépinay et al. measured vectorial force fields and force field derivatives arising from the electrostatic interaction of a voltage-biased metallic sample of pyramidal shape with a NW cantilever[16]. The authors furthermore reconstructed a

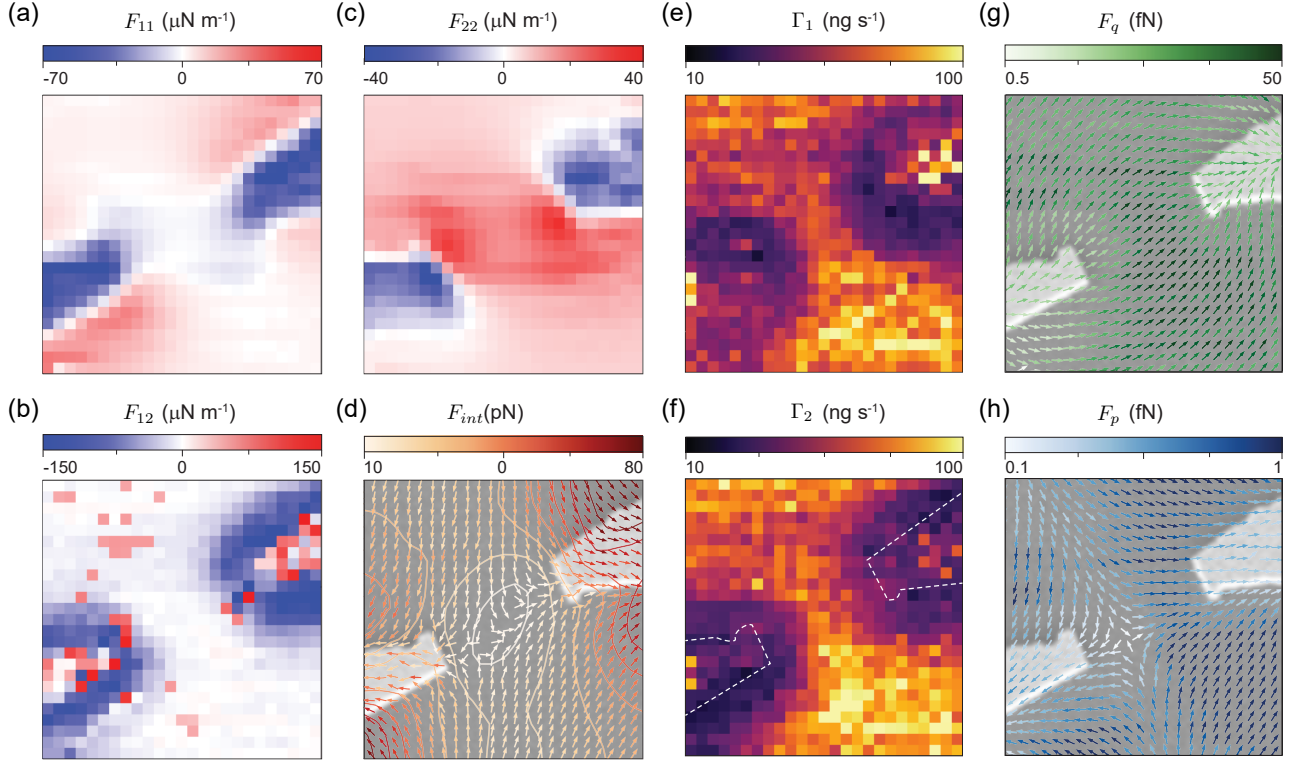


Figure 8: (a-c) Measurements of F_{11} , F_{12} , and F_{22} tip-sample force derivatives as a function of NW tip position over patterned sample surface. The scale bar corresponds to $1 \mu\text{m}$ (d) Vector plot of in-plane force field derived by numerically integrating the derivatives of (a-c). The plot is overlaid on a scanning electron micrograph of the sample with patterned gate electrodes. (e), (f) Dissipation of each orthogonal mode as a function of NW tip position. (g) Vector plot of \mathbf{F}_q induced by gate electric field on the charged NW. (h) Vector plot of \mathbf{F}_p induced by gate electric field on the polarizable NW. Adapted from Ref.[9].

three-dimensional image of the force field derivatives by scanning the NW vertically away from the sample, up to a tip-sample distance of several microns.

C. Magnetic force microscopy

In recent years, there has been a flurry of activity in developing nanometer-scale magnetic imaging technology. These efforts are driven by a number outstanding questions in spintronics – such as how to control magnetic skyrmions – and in mesoscopic transport – such as how current flows in topological insulators and two-dimensional materials. Scanning probe microscopy, in particular, has made remarkable improvements in both the sensitivity and resolution of magnetic imaging. Some of the most successful tools are magnetic force microscopy (MFM), spin-polarized scanning tunneling microscopy, as well as scanning magnetometers based on nitrogen-vacancy centers in diamond, Hall-bars, and superconducting quantum interference devices (SQUIDs). Despite this progress, it is now becoming clear that nanomechanical sensors, in general, and NWs in particular, provide a huge untapped opportunity in magnetic sensing.

The first magnetic SPM, MFM, was introduced in the late 1980s as a natural extension of AFM. These days, it is performed in air, liquid, vacuum, and at a variety of temperatures. Under ideal conditions, state-of-the-art MFM can reach spatial resolutions down to 10 nm [84], though more typically around 100 nm . In 2009, its application to magnetic resonance, magnetic resonance force microscopy (MRFM), resulted in the first demonstration of three-dimensional nuclear magnetic resonance imaging (MRI) with nanometer-scale resolution [85].

NW scanning force sensors with proper functionalization of their tips, can be used to measure weak magnetic forces. Recent experiments have shown that a NW’s high force sensitivity – when combined with a highly concentrated and strongly magnetized tip – gives it an exquisite sensitivity to magnetic field gradients [11]. Using a MnAs-tipped GaAs NW, the authors demonstrated a sensitivity to $11 \text{ mT}/\text{m}\sqrt{\text{Hz}}$. Having quantified the NW’s response to magnetic field gradients, the authors calculate its sensitivity to other magnetic field sources, including a magnetic moment (dipole field), a superconducting vortex (monopole field), or an infinitely long and thin line of current [86]. In particular, they expect a moment sensitivity of $54 \mu_B/\sqrt{\text{Hz}}$, a flux sensitivity of $1.3 \mu\Phi_0/\sqrt{\text{Hz}}$,

and line-current sensitivity of $9 \text{ nA}/\sqrt{\text{Hz}}$ at a tip-sample spacing of 250 nm. Such sensitivities compare favorably to those of other magnetic microscopies, including scanning Hall microscopy, magneto-optic microscopy, scanning SQUID microscopy, and scanning nitrogen-vacancy magnetometry. Furthermore, magnet-tipped NWs have a huge potential for improvement as probes of weak magnetic field patterns if tips sizes and tip-sample spacings can be further reduced.

In addition to improved sensitivity, NW MFM provides other potential advantages compared to conventional MFM. First, scanning in the pendulum geometry with the NW oscillating in the plane of the sample has the characteristics of lateral MFM. This technique, which is realized with the torsional mode of a conventional cantilever, distinguishes itself from the more commonly used tapping-mode MFM in its ability to produce magnetic images devoid of spurious topography-related contrast and in a demonstrated improvement in lateral spatial resolution of up to 15% [87]. Second, the nanometer-scale magnetic particle at the apex of the NW force sensor minimizes the size of the MFM tip, allowing for optimal spatial resolution and minimal perturbation of the investigated sample.

There have been a number of efforts at creating high-resolution MFM tips on conventional cantilevers, including attaching coated CNT tips [88], milling tips by FIB [89], or using electron beam induced deposition techniques [90, 91]. Despite this work, non-invasive, high-resolution MFM tips are still needed. In particular, the tips with the smallest volumes realized thus far, tend to have rather undefined magnetization directions due to amorphous magnetic materials and nearly symmetric particle shape. Recent results show that small single crystal magnetic particles with defined and predictable magnetization directions can be realized atop a single NW [11, 92]. In particular, Rossi et al. carried out measurements of dynamic cantilever magnetometry [60, 93, 94] to extract the magnetic properties of each MnAs tip from the mechanical response of the NW to a uniform external magnetic field. These measurements, along with measurements of the NW's response to a well-known magnetic field profile generated by a lithographically patterned wire, confirmed that in remanence the magnetic tips are – in most cases – strongly magnetized and dipole-like. Fig. 9a and b show the experimental setup in which the magnet-tipped NW is scanned across a current-carrying wire. An SEM of the MnAs magnetic tip is shown in Fig. 9 c. The magnetic force measured along the two mode directions is shown in Fig. 9 d, showing a response consistent with a remanent dipole-like magnetic tip. These results bode well for the resolution possible with NW MFM probes. In principle, as discussed by van Schendel et al., detailed analysis of MFM tips shows that the closer a tip approaches an ideal magnetic dipole, the better its sensitivity to high spatial frequencies, and therefore the higher its potential resolution [95].

The prospect of increased sensitivity and resolution,

combined with few restrictions on operating temperature, make NW MFM ideally suited to investigate nanometer-scale spin textures, skyrmions, superconducting and magnetic vortices, as well as ensembles of electronic or nuclear spins. Non-invasive magnetic tips may also open opportunities to study current flow in 2D materials and topological insulators. The ability of a NW sensor to map all in-plane spatial force derivatives [9, 16] should provide fine detail of stray field profiles above magnetic and current carrying samples, in turn providing detailed information on the underlying phenomena. Directional measurements of dissipation may also prove useful for visualizing domain walls and other regions of inhomogeneous magnetization. As shown by Grütter et al., dissipation contrast, which maps the energy transfer between the tip and the sample, strongly depends on the sample's nanometer-scale magnetic structure [3].

D. Magnetic resonance force microscopy

So far, the most developed application for magnetic force sensing with NWs has been MRFM for nanometer-scale magnetic resonance imaging (nano-MRI). The method relies on an ultra-sensitive mechanical force sensor to detect the magnetic resonance from tiny ensembles of nuclear spins.

Conventional MRI techniques employ pick-up coils to detect the small changes in magnetic field induced by flipping nuclear moments contained in a sample. These magnetic signals are so weak that conventional instruments cannot resolve objects smaller than several micrometers – about the size of a small cell [96]. MRFM improves on this sensitivity by mechanically detecting the magnetic forces produced by nuclear moments. A mechanical resonator is used to sense the forces arising between nuclear moments in a sample and a nearby source of magnetic field gradient. In MRFM, RF pulses cause nuclear moments in a sample to periodically flip, generating an oscillating force on the mechanical resonator. These alternating forces, in turn, drive the resonator to oscillate. Force-detected MRI is more sensitive to nanometer-scale samples than conventional techniques because much smaller detectors can be made. For the inductive technique to be sensitive, the size of the pick-up coil must be similar to the size of the sample. For nanometer-scale samples, this is practically impossible. On the other hand, high-quality cantilevers can have dimensions far below a micrometer such that the sample mass is significant compared to the bare resonator mass. Such mechanical transducers enabled the current state-of-the-art force-detected nano-MRI, which was demonstrated by Degen et al. in 2009 [85]. In this work, researchers captured 3D images of individual tobacco mosaic virus (TMV) particles with a resolution better than 10 nm along each dimension. The technique has the unique capability to image the interior of nanometer-scale objects non-invasively and with intrinsic chemical selectivity. Despite a number of further

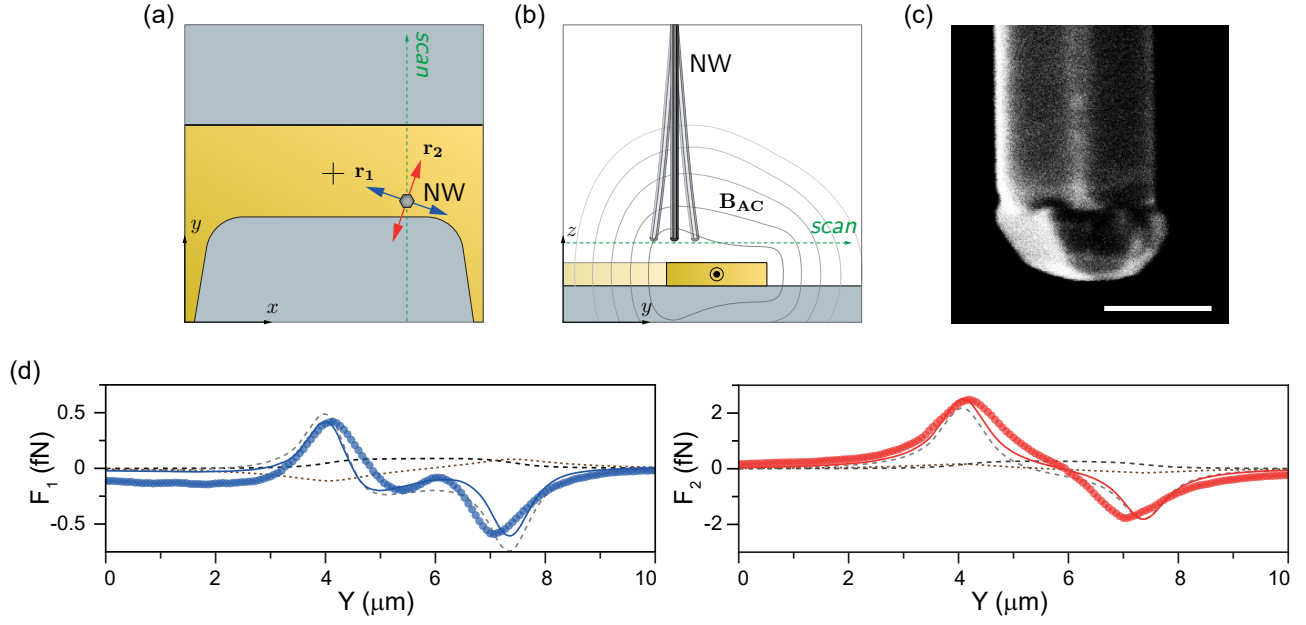


Figure 9: (a), (b) Schematic illustration of MFM experiment with NW cantilever and current-carrying Au wire. The NW scan direction used to produced measurements in (c) is indicated by the green line in top view (a) and side view (b). B_{AC} corresponds to the magnetic field produced by the alternating current in the wire, B to an externally applied magnetic field. (c) Scanning electron micrograph of the tip of a GaAs NW featuring a MnAs segment at the end. The scalebar corresponds to 100 nm. (d) Plots of the measured (dotted line) and calculated (solid line) forces driving the first (blue) and the second (red) mode over the line scan indicated in (a) and (b). For each plot three distinct drive contributions are shown as dashed lines: the monopole (black), dipole (gray) and torque (magenta) terms. Adapted from Ref.[11].

refinements and demonstrations [97, 98], improvements in MRFM sensitivity and resolution have stalled in recent years, leaving a number of technical obstacles to be overcome for the technique to become a useful tool for biologists and materials scientists.

Foremost among these obstacles is the reduction in the mechanical dissipation of the cantilever sensor. Lower mechanical dissipation would yield better force sensitivities and therefore sensitivity to smaller numbers of nuclear spins. Such an improvement would result in nano-MRI with improved resolution. In the last few years, the development and application of NW cantilevers to MRFM has been making promising steps in this direction. In 2012, Nichol et al. used a Si NW force transducer in an MRFM experiment detecting ^1H in a nanometer-scale polystyrene sample [6]. During the measurements they achieved a thermally limited force sensitivity of around $1 \text{ aN}/\sqrt{\text{Hz}}$ at a spacing of 80 nm from the surface at 8 K, which is significantly lower than was measured at 300 mK in the TMV experiment [85]. This improvement is largely due to the ultra-low native dissipation of the NWs in comparison to top-down ultrasensitive cantilever and to their drastically reduced surface dissipation. In fact, Nichol et al., show that at a tip-surface spacing of 7 nm, a typical Si NW experiences nearly a factor of 80 less surface dissipation and factor of 250 less total dissipation than audio frequency cantilevers under similar conditions. The mechanisms behind this difference are

not completely clear; the small cross-sectional area of a NW may decrease its coupling to the surface or, perhaps, the spectral density of surface fluctuations is lower at the MHz resonant frequencies of the NWs than at the kHz resonant frequencies of the cantilevers.

This ground-breaking work established NW oscillators as ultrasensitive cantilevers for MRFM detection. The measurement protocol that was developed for the NW transducers uses a nanoscale current-carrying wire to generate both time-dependent RF magnetic fields and time-dependent magnetic field gradients. This protocol, known as MAGGIC, may ultimately open new avenues for nanoscale magnetic resonance imaging with more favorable SNR properties [7].

Given that nanometer-scale MRFM requires intense static magnetic field gradients, both NMR spectroscopy and uniform spin manipulation using RF pulses have always been difficult to implement in such measurements. As a result, MRFM experiments often rely on inherently slow adiabatic passage pulses, which limited the mechanical transducer to resonance frequencies in the few kHz regime. In addition, conventional pulsed magnetic resonance techniques cannot be applied to nanometer-scale MRFM because statistical spin fluctuations often exceed the Boltzmann spin polarization [99]. In this regime, the projection of the sample magnetization along any axis fluctuates randomly in time.

In their article, Nichol et al. presented a new paradigm

in force-detected magnetic resonance that overcomes both challenges to enable pulsed nuclear magnetic resonance in nanometer-size statistically polarized samples. The first challenge was solved by using the nanometer-scale constriction to generate both large RF fields and large magnetic field gradients. In this way, the authors were able to turn their magnetic field gradients on and off at will. The method allowed the use of high-frequency mechanical resonances, such as those provided by a NW. Using a scheme similar to conventional MRI, switchable gradients in static and RF field encoded the Fourier transform of the 2D spin density into their spin signal. As a result, they were able to reconstruct a 2D projection of the ^1H density in a polystyrene sample with roughly 10-nm resolution. The protocol was able to function in the statistically polarized regime because the authors periodically applied RF pulses, which create correlations in the statistical polarization of a solid organic sample. The spin-noise correlations were then read-out using gradient pulses generated by ultra-high current densities in the nanoscale metal constriction. The authors also showed that Fourier-transform imaging enhances sensitivity via the multiplex advantage for high-resolution imaging of statistically polarized samples. Most importantly, the protocol established a method by which all other pulsed magnetic resonance techniques can be used for nanoscale imaging and spectroscopy. Recent work by Rose et al., combines the high spin sensitivity of NW-based magnetic resonance detection with high-spectral-resolution NMR spectroscopy [8]. The authors make use of the resulting enhancement in nuclear spin coherence times to perform Fourier-transform imaging of proton spins with a one-dimensional slice thickness below 2 nm.

Given the potential for even more sensitive NW transducers, these proof-of-concept experiments bode well for increasing nano-MRI sensitivity and resolution. Even without improvement in sensitivity, the authors' technique could also be extended to enable full 3D encoding with constrictions capable of producing two orthogonal static gradients [100]. More generally, the approach serves as a model for applying sophisticated pulsed magnetic resonance schemes from conventional MRI to the nanometer-scale version.

V. OUTLOOK

The application of NW cantilevers as sensitive force transducers is in the early stages. Nevertheless, the demand for more sensitive techniques has positioned nanometer-scale mechanical structures – and NWs in particular – as the transducers of the future. At present, the promise of these devices has been demonstrated in a small number of proof-of-concept experiments. As discussed in this review, these methods and applications demonstrate the capabilities of NW transducers and their unique advantages, especially in the detection of weak

forces. Nevertheless, much work remains to be done before NWs become part of the standard tool-box of scanning probe microscopies.

Force sensitivity can undoubtedly be improved by developing longer and thinner NW transducers. So far, researchers have not made concerted efforts to optimize NW geometry, leaving much to be gained by such work. Better spatial resolutions could also be achieved by developing NWs with sharper tips, through, for example, specialized growth techniques or by focussed ion beam milling. By carrying out SPM experiments with such sharp NWs in ultra-high vacuum conditions, atomic resolution should be possible. Combined with its vectorial force sensing capability, such a NW scanning probe could be used to reveal the anisotropy of atomic bonding forces.

Higher force sensitivity would also translate into more sensitive measurements of dissipation and non-contact friction. AFM in the pendulum geometry – the same geometry used for NWs – is ideally suited to measurements of nanometer-scale dissipation. Such measurements have recently been used to detect superconducting [4] and bulk structural phase transitions [101]. They can also shed light on concepts such as superlubricity, atomic-scale friction, and quantum friction [102]. Furthermore, energy dissipation plays a central role in the breakdown of topological protection, the loss of quantum information, and disorder-assisted hot electrons scattering in graphene [103]. The ability to map tip-sample force fields and energy losses makes NW transducers ideal for investigating how and where energy leaks.

Finally, the combination of high force sensitivity, high spatial resolution, and low invasiveness of magnetic NW probes has the potential to expand the applicability of MFM. Such sensors could image the stray field thin ferromagnetic layers and other magnetic nanostructures hosting non-uniform states too fragile for conventional MFM. For such applications, efforts must first focus on producing smaller magnetic tips. Alternatively, the production of different types of magnet-tipped NWs could be attempted, through the evaporation of magnetic caps on sharp non-magnetic NWs or by direct focused ion beam induced deposition. By combining NW transducers with ferromagnetic resonance techniques, the spatial imaging of spin waves and the dynamics of individual skyrmions may also become possible.

-
- [1] Gloppe A, Verlot P, Dupont-Ferrier E, Siria A, Poncharal P, Bachelier G, Vincent P and Arcizet O 2014 *Nature Nanotechnology* **9** 920–926 ISSN 1748-3387
- [2] Thillozen N, Sebald K, Hardtdegen H, Meijers R, Calarco R, Montanari S, Kaluza N, Gutowski J and Lüth H 2006 *Nano Letters* **6** 704–708 ISSN 1530-6984
- [3] Grütter P, Liu Y, LeBlanc P and Dürig U 1997 *Applied Physics Letters* **71** 279–281 ISSN 0003-6951
- [4] Kisiel M, Gnecco E, Gysin U, Marot L, Rast S and Meyer E 2011 *Nature Materials* **10** 119–122 ISSN 1476-4660
- [5] Cockins L, Miyahara Y, Bennett S D, Clerk A A and Grutter P 2012 *Nano Letters* **12** 709–713 ISSN 1530-6984
- [6] Nichol J M, Hemesath E R, Lauhon L J and Budakian R 2012 *Physical Review B* **85** 054414
- [7] Nichol J M, Naibert T R, Hemesath E R, Lauhon L J and Budakian R 2013 *Physical Review X* **3** 031016
- [8] Rose W, Haas H, Chen A Q, Jeon N, Lauhon L J, Cory D G and Budakian R 2018 *Physical Review X* **8** 011030
- [9] Rossi N, Braakman F R, Cadeddu D, Vasyukov D, Tütüncüoğlu G, Fontcuberta i Morral A and Poggio M 2017 *Nature Nanotechnology* **12** 150–155 ISSN 1748-3387
- [10] Braakman F R, Rossi N, Tütüncüoğlu G, i Morral A F and Poggio M 2018 *Physical Review Applied* **9** 054045
- [11] Rossi N, Gross B, Dirnberger F, Bougeard D and Poggio M 2018
- [12] Cadeddu D, Braakman F R, Tütüncüoğlu G, Matteini F, Rüffer D, Fontcuberta i Morral A and Poggio M 2016 *Nano Letters* **16** 926–931 ISSN 1530-6984
- [13] Montinaro M, Wüst G, Munsch M, Fontana Y, Russo-Averchi E, Heiss M, Fontcuberta i Morral A, Warburton R J and Poggio M 2014 *Nano Letters* **14** 4454–4460 ISSN 1530-6984
- [14] Foster A P, Maguire J K, Bradley J P, Lyons T P, Krysa A B, Fox A M, Skolnick M S and Wilson L R 2016 *Nano Letters* ISSN 1530-6984
- [15] Pairis S, Donatini F, Hocevar M, Tumanov D, Vaish N, Claudon J, Poizat J P and Verlot P 2018 *arXiv:1803.09312 [cond-mat]* (Preprint 1803.09312)
- [16] de Lépinay L M, Pigeau B, Besga B, Vincent P, Poncharal P and Arcizet O 2017 *Nature Nanotechnology* **12** 156–162 ISSN 1748-3387
- [17] de Lépinay L M, Pigeau B, Besga B and Arcizet O 2018 *Nature Communications* **9** 1401 ISSN 2041-1723
- [18] Perisanu S, Vincent P, Ayari A, Choueib M, Purcell S T, Bechelany M and Cornu D 2007 *Applied Physics Letters* **90** 043113 ISSN 0003-6951, 1077-3118
- [19] Perisanu S, Barois T, Ayari A, Poncharal P, Choueib M, Purcell S T and Vincent P 2010 *Physical Review B* **81** 165440
- [20] Pigeau B, Rohr S, Mercier de Lépinay L, Gloppe A, Jacques V and Arcizet O 2015 *Nature Communications* **6** ISSN 2041-1723
- [21] Nichol J M, Hemesath E R, Lauhon L J and Budakian R 2008 *Applied Physics Letters* **93** 193110 ISSN 0003-6951, 1077-3118
- [22] Nichol J M, Hemesath E R, Lauhon L J and Budakian R 2009 *Applied Physics Letters* **95** 123116 ISSN 0003-6951
- [23] Gil-Santos E, Ramos D, Martínez J, Fernández-Regúlez M, García R, San Paulo A, Calleja M and Tamayo J 2010 *Nature Nanotechnology* **5** 641–645 ISSN 1748-3387
- [24] Gil-Santos E, Ramos D, Pini V, Llorens J, Fernández-Regúlez M, Calleja M, Tamayo J and Paulo A S 2013 *New Journal of Physics* **15** 035001 ISSN 1367-2630
- [25] Ramos D, Gil-Santos E, Pini V, Llorens J M, Fernández-Regúlez M, San Paulo A, Calleja M and Tamayo J 2012 *Nano Letters* **12** 932–937 ISSN 1530-6984
- [26] Ramos D, Gil-Santos E, Malvar O, Llorens J M, Pini V, Paulo A S, Calleja M and Tamayo J 2013 *Scientific Reports* **3** ISSN 2045-2322
- [27] Belov M, Quitoriano N J, Sharma S, Hiebert W K, Kamins T I and Evoy S 2008 *Journal of Applied Physics* **103** 074304 ISSN 0021-8979, 1089-7550
- [28] Feng X L, He R, Yang P and Roukes M L 2007 *Nano Letters* **7** 1953–1959 ISSN 1530-6984
- [29] Siria A and Niguès A 2017 *Scientific Reports* **7** 11595 ISSN 2045-2322
- [30] Tavernarakis A, Stavrinadis A, Nowak A, Tsioutsios I, Bachtold A and Verlot P 2018 *Nature Communications* **9** 662 ISSN 2041-1723
- [31] Tsioutsios I, Tavernarakis A, Osmond J, Verlot P and Bachtold A 2017 *Nano Letters* **17** 1748–1755 ISSN 1530-6984
- [32] Cleland A N 2003 *Foundations of Nanomechanics From Solid-State Theory to Device Applications* (Berlin, Heidelberg: Springer Berlin Heidelberg) ISBN 978-3-662-05287-7 3-662-05287-3
- [33] Poot M and van der Zant H S J 2012 *Physics Reports* **511** 273–335 ISSN 0370-1573
- [34] Reif F 1965 *Fundamentals of Statistical and Thermal Physics* McGraw-Hill series in fundamentals of physics (New York [etc.]: McGraw-Hill) ISBN 978-0-07-051800-1
- [35] Kubo R 1966 *Reports on Progress in Physics* **29** 255 ISSN 0034-4885
- [36] Robins W P 1982 *Phase Noise in Signal Sources : (Theory and Applications)* IEE telecommunications series (London: Peregrinus) ISBN 978-0-906048-76-4
- [37] Sansa M, Sage E, Bullard E C, Gély M, Alava T, Colinet E, Naik A K, Villanueva L G, Duraffourg L, Roukes M L, Jourdan G and Hentz S 2016 *Nat Nano* **11** 552–558 ISSN 1748-3387
- [38] Moser J, Güttinger J, Eichler A, Esplandiu M J, Liu D E, Dykman M I and Bachtold A 2013 *Nature Nanotechnology* **8** 493–496 ISSN 1748-3387
- [39] Faust T, Rieger J, Seitner M J, Krenn P, Kotthaus J P and Weig E M 2012 *Physical Review Letters* **109** 037205
- [40] Faust T, Rieger J, Seitner M J, Kotthaus J P and Weig E M 2013 *Nature Physics* **9** 485–488 ISSN 1745-2473
- [41] Spreeuw R J C, van Druten N J, Beijersbergen M W, Eliel E R and Woerdman J P 1990 *Physical Review Letters* **65** 2642–2645
- [42] Okamoto H, Gourgout A, Chang C Y, Onomitsu K, Mahboob I, Chang E Y and Yamaguchi H 2013 *Nature Physics* **9** 480–484 ISSN 1745-2473
- [43] Degen C L, Reinhard F and Cappellaro P 2017 *Reviews of Modern Physics* **89** 035002
- [44] Braakman F R, Cadeddu D, Tütüncüoğlu G, Matteini F, Rüffer D, i Morral A F and Poggio M 2014 *Applied Physics Letters* **105** 173111 ISSN 0003-6951, 1077-3118

- [45] Eichler A, Heugel T L, Leuch A, Degen C L, Chitra R and Zilberberg O 2018 *Applied Physics Letters* **112** 233105 ISSN 0003-6951
- [46] da Silva M R M C and Glynn C C 1978 *Journal of Structural Mechanics* **6** 449–461 ISSN 0360-1218
- [47] da Silva M R M C and Glynn C C 1978 *Journal of Structural Mechanics* **6** 437–448 ISSN 0360-1218
- [48] Schmid S, Villanueva L G and Roukes M L 2016 *Fundamentals of Nanomechanical Resonators* (Springer International Publishing) ISBN 978-3-319-28689-1
- [49] Cadeddu D *Nanomechanics and Scanning Probe Microscopy with Nanowires* Ph.D. thesis
- [50] Lifshitz R and Cross M C *Review of nonlinear dynamics and complexity* **1** 1–52
- [51] Eichler A, Moser J, Chaste J, Zdrojek M, Wilson-Rae I and Bachtold A 2011 *Nature Nanotechnology* **6** 339–342 ISSN 1748-3395
- [52] Rugar D and Hansma P 2008 *Physics Today* **43** 23 ISSN 0031-9228
- [53] Akamine S, Barrett R C and Quate C F 1990 *Applied Physics Letters* **57** 316–318 ISSN 0003-6951
- [54] González G I and Saulson P R 1994 *The Journal of the Acoustical Society of America* **96** 207–212 ISSN 0001-4966
- [55] Cagnoli G, Hough J, DeBra D, Fejer M M, Gustafson E, Rowan S and Mitrofanov V 2000 *Physics Letters A* **272** 39–45 ISSN 0375-9601
- [56] Tsaturyan Y, Barg A, Polzik E S and Schliesser A 2017 *Nature Nanotechnology* **advance online publication** ISSN 1748-3387
- [57] Ghadimi A H, Fedorov S A, Engelsen N J, Bereyhi M J, Schilling R, Wilson D J and Kippenberg T J 2018 *Science* **360** 764–768 ISSN 0036-8075, 1095-9203
- [58] Marshall W, Simon C, Penrose R and Bouwmeester D 2003 *Physical Review Letters* **91** 130401
- [59] Rugar D, Stipe B C, Mamin H J, Yannoni C S, Stowe T D, Yasumura K Y and Kenny T W 2001 *Applied Physics A* **72** S3–S10 ISSN 0947-8396, 1432-0630
- [60] Stipe B C, Mamin H J, Stowe T D, Kenny T W and Rugar D 2001 *Physical Review Letters* **86** 2874–2877 00111
- [61] Tao Y, Navaretti P, Hauert R, Grob U, Poggio M and Degen C L 2015 *Nanotechnology* **26** 465501 ISSN 0957-4484
- [62] Stipe B C, Mamin H J, Stowe T D, Kenny T W and Rugar D 2001 *Physical Review Letters* **87** 096801
- [63] Kuehn S, Loring R F and Marohn J A 2006 *Physical Review Letters* **96** 156103
- [64] Sazonova V, Yaish Y, Üstünel H, Roundy D, Arias T A and McEuen P L 2004 *Nature* **431** 284–287 ISSN 0028-0836
- [65] Bunch J S, van der Zande A M, Verbridge S S, Frank I W, Tanenbaum D M, Parpia J M, Craighead H G and McEuen P L 2007 *Science* **315** 490–493 ISSN 0036-8075, 1095-9203
- [66] Moser J, Eichler A, Güttinger J, Dykman M I and Bachtold A 2014 *Nature Nanotechnology* **advance online publication** ISSN 1748-3387
- [67] Gysin U, Rast S, Kisiel M, Werle C and Meyer E 2011 *Review of Scientific Instruments* **82** 023705 ISSN 0034-6748, 1089-7623
- [68] Sekaric L, Carr D W, Evoy S, Parpia J M and Craighead H G 2002 *Sensors and Actuators A: Physical* **101** 215–219 ISSN 0924-4247
- [69] Azak N O, Shagam M Y, Karabacak D M, Ekinci K L, Kim D H and Jang D Y 2007 *Applied Physics Letters* **91** 093112 ISSN 0003-6951
- [70] Li M, Bhiladvala R B, Morrow T J, Siooss J A, Lew K K, Redwing J M, Keating C D and Mayer T S 2008 *Nature Nanotechnology* **3** 88–92 ISSN 1748-3387
- [71] Favero I, Stapfner S, Hunger D, Paulitschke P, Reichel J, Lorenz H, Weig E M and Karrai K 2009 *Optics Express* **17** 12813 ISSN 1094-4087
- [72] Tanner S M, Gray J M, Rogers C T, Bertness K A and Sanford N A 2007 *Applied Physics Letters* **91** 203117 ISSN 0003-6951
- [73] He R, Feng X L, Roukes M L and Yang P 2008 *Nano Letters* **8** 1756–1761 ISSN 1530-6984
- [74] Truitt P A, Hertzberg J B, Huang C C, Ekinci K L and Schwab K C 2007 *Nano Letters* **7** 120–126 ISSN 1530-6984
- [75] Sanii B and Ashby P D 2010 *Physical Review Letters* **104** 147203
- [76] Fu C, Deng W, Zou L, Zhu W, Wang N and Xue F 2017 *arXiv:1711.04446 [cond-mat]* (Preprint 1711.04446)
- [77] Weymouth A J 2017 *Journal of Physics: Condensed Matter* **29** 323001 ISSN 0953-8984
- [78] Pfeiffer O, Bennewitz R, Baratoff A, Meyer E and Grütter P 2002 *Physical Review B* **65** 161403
- [79] Giessibl F J, Herz M and Mannhart J 2002 *Proceedings of the National Academy of Sciences* **99** 12006–12010 ISSN 0027-8424, 1091-6490
- [80] Kawai S, Kitamura S i, Kobayashi D and Kawakatsu H 2005 *Applied Physics Letters* **87** 173105 ISSN 0003-6951, 1077-3118
- [81] Kawai S, Sasaki N and Kawakatsu H 2009 *Physical Review B* **79** 195412
- [82] Kawai S, Glatzel T, Koch S, Such B, Baratoff A and Meyer E 2010 *Physical Review B* **81** 085420
- [83] Vilhena J G and Pérez R 2018 *Nature Materials* **17** 852 ISSN 1476-4660
- [84] Schmid I, Marioni M A, Kappenberger P, Romer S, Parlinska-Wojtan M, Hug H J, Hellwig O, Carey M J and Fullerton E E 2010 *Physical Review Letters* **105** 197201
- [85] Degen C L, Poggio M, Mamin H J, Rettner C T and Rugar D 2009 *Proceedings of the National Academy of Sciences* **106** 1313–1317 ISSN 0027-8424, 1091-6490
- [86] Kirtley J R 2010 *Reports on Progress in Physics* **73** 126501 ISSN 0034-4885
- [87] Kaidatzis A and García-Martín J M 2013 *Nanotechnology* **24** 165704 ISSN 0957-4484
- [88] Deng Z, Yenilmez E, Leu J, Hoffman J E, Straver E W J, Dai H and Moler K A 2004 *Applied Physics Letters* **85** 6263–6265 ISSN 0003-6951
- [89] Phillips G N, Siekman M, Abelmann L and Lodder J C 2002 *Applied Physics Letters* **81** 865–867 ISSN 0003-6951
- [90] Lau Y M, Chee P C, Thong J T L and Ng V 2002 *Journal of Vacuum Science & Technology A: Vacuum, Surfaces, and Films* **20** 1295–1302 ISSN 0734-2101
- [91] Koblischka M R, Hartmann U and Sulzbach T 2003 *Thin Solid Films* **428** 93–97 ISSN 0040-6090
- [92] Hubmann J, Bauer B, Körner H S, Furthmeier S, Buchner M, Bayreuther G, Dirnberger F, Schuh D, Back C H, Zweck J, Reiger E and Bougeard D 2016 *Nano Letters* **16** 900–905 ISSN 1530-6984
- [93] Rossel C, Bauer P, Zech D, Hofer J, Willemin M and

- Keller H 1996 *Journal of Applied Physics* **79** 8166–8173 ISSN 0021-8979, 1089-7550
- [94] Harris J G E, Awschalom D D, Matsukura F, Ohno H, Maranowski K D and Gossard A C 1999 *Applied Physics Letters* **75** 1140–1142 ISSN 0003-6951, 1077-3118
- [95] van Schendel P J A, Hug H J, Stiefel B, Martin S and Güntherodt H J 2000 *Journal of Applied Physics* **88** 435–445 ISSN 0021-8979, 1089-7550
- [96] Ciobanu L, Seeber D A and Pennington C H 2002 *Journal of Magnetic Resonance* **158** 178–182 ISSN 1090-7807
- [97] Poggio M and Degen C L 2010 *Nanotechnology* **21** 342001 ISSN 0957-4484 00041
- [98] Poggio M and Herzog B E 2018 Force-Detected Nuclear Magnetic Resonance *Micro and Nano Scale NMR* (Wiley-Blackwell) pp 381–420 ISBN 978-3-527-69728-1
- [99] Herzog B E, Cadeddu D, Xue F, Peddibhotla P and Poggio M 2014 *Applied Physics Letters* **105** 043112 ISSN 0003-6951, 1077-3118
- [100] Nichol J 2014 *Nanoscale Magnetic Resonance Imaging Using Silicon Nanowire Oscillators* Ph.D. thesis University of Illinois at Urbana-Champaign 00000
- [101] Kisiel M, Pellegrini F, Santoro G E, Samadashvili M, Pawlak R, Benassi A, Gysin U, Buzio R, Gerbi A, Meyer E and Tosatti E 2015 *Physical Review Letters* **115** 046101
- [102] Volokitin A I and Persson B N J 2011 *Physical Review Letters* **106** 094502
- [103] Halbertal D, Cuppens J, Shalom M B, Embon L, Shadmi N, Anahory Y, Naren H R, Sarkar J, Uri A, Ronen Y, Myasoedov Y, Levitov L S, Joselevich E, Geim A K and Zeldov E 2016 *Nature* **539** 407–410 ISSN 0028-0836